Supplementary Materials for

Sub-millimeter fiberscopic robot with integrated maneuvering, imaging, and biomedical operation abilities

Tieshan Zhang[1,2,3†], Gen Li[1,2,3†], Hao Ren[2], Liu Yang[1,3], Xiong Yang[1,3], Rong Tan[1,3], Yifeng Tang[2], Dong Guo[2], Haoxiang Zhao[1,3], Wanfeng Shang[4,5], Yajing Shen[1,3*]

1 Department of Electronic and Computer Engineering, Hong Kong University of Science and Technology, Hong Kong SAR 999077, China
2 The Robot and Automation Center and the Department of Biomedical Engineering, City University of Hong Kong, Hong Kong SAR 999077, China
3 Center on Smart Manufacturing, Hong Kong University of Science and Technology, Hong Kong SAR 999077, China
4 National Engineering Laboratory of Big Data System Computing Technology, Shenzhen University, 518060 Baishi Road, Nanshan District, Shenzhen, China
5 Shenzhen Institute of Advanced Technology (SIAT), Chinese Academy of Science (CAS), Xueyuan Boulevard 1068, Nanshan, Shenzhen, 518055, P.R.China

Corresponding author: Yajing Shen. Email: eeyajing@ust.hk
These authors contributed equally: Tieshan Zhang, Gen Li

This file includes:

Supplementary Text

Supplementary Note S1. Additional information about the fabrication procedures

As shown in Fig. S1, the fabrication process of the proposed fiberscopic robot can be roughly divided into three main steps, including the main body construction (Fig. S1a,b), magnetic elastomer formation(Fig. S1c,d), and hydrogel skin generation(Fig. S1e,f). The overall manufacturing results are quite reliable if the fabrication process can be strictly followed.

(1) Fabrication details: To help the researcher reproduce this result, here we list some key points needed to pay attention during the fabrication.
a. Main body construction: (i) Due to the hollow structure, the printed skeleton may encounter geometrical deformation during the printing procedure. It is necessary to attach enough detachable supports to the structure in the slicing software. (ii) Due to the deep-hole structure, there could retain resin residues inside that induce difficulty in component insertion. Please check the residue and carry out further clean after the printing if necessary. (iii) During the assembly procedure of the fiber array, it is essential to manually insert slowly to prevent damage. (iv) After the successful insertion of the fiber array, each fiber would be slightly adjusted to achieve the parallel assembly.
b. Magnetic elastomer formation: To form the magnetic elastomer, we here utilize a self-developed technology of magnetic spray[1]. (i) Due to the viscosity of the elastomer matrix, it is necessary to stir the mixture efficient to achieve a homogeneous status. (ii) With quick and high-pressure spraying, the obtained magnetic skin would obtain a relatively uniform state.
c. Hydrogel skin generation: The generated hydrogel skin could ensure relatively high consistency by following the detailed procedures shown in Ref 15.

(2) Materials safety: Considering the safety utilization of the materials, the utilized photosensitive resins from BMF Material Technology Inc. are known as a type of material with long-term stability and biocompatibility , making them suitable for fabricating various biomedical devices[2-4]. Besides, the elastomer we utilized is also a common type of biocompatible silicone rubber that has been widely applied in fabrication of biomedical robots/devices[5-7]. Lastly, the hydrogel we employed has demonstrated the capability of antifouling and bacterial adhesion resistance[8]. Therefore, the utilized materials can well guarantee the safety.

(3) Dimensional tolerance: Regarding the dimensional tolerances of the entire manufacturing process, the measured diameter ranges of the printed skeleton, the magnetic elastomer, and the hydrogel skin are about 740-760μm, 880-920μm, and 940-960 μm, respectively, showing a good uniformity.

(4) Fragile performance: As for the fragile performance, we utilized the bare optical fiber with the glass core and glass cladding (OD: 125 μm) while removing the outer coating/buffer layer (Fig. S2, OD: 220 μm) and tested the minimal bending radius of the optical fiber at about 3.38 mm, as shown in Fig. S3a. To protect the fiber array, we coated the outer surface of the long rear body of the probe robot with a

thin layer of elastomer and hydrogel skin (Fig. 1, Fig. S1). In this case, the assembled probe robot can still show a small bending radius of about 5.58 mm (Fig. S3b). This value is about five times smaller than most reported traditional endoscopes (~30 mm)[9-11] and even smaller than that of the ultra-fine micro borescope (~6.0 mm) [12,13]. Consequently, the fabricated probe robot can show its bright application potential in practical scenarios.

(5) Fixation performance of the UV glue: The fixation performance of the UV glue has been tested comprehensively. Firstly, we attempted to manually tear the skeleton from the fiber array but failed, confirming the strong fixation of the UV glue. Next, we immersed the assembly in a hydrogel solution to generate the outer hydrogel skin. The skeleton remained well-fixed to the fiber array, further verifying the glue's effectiveness. Additionally, after ex-vivo experiments in a porcine lung bronchial channel environment, the skeleton withstood manual tear tests, demonstrating excellent fixation performance under humid conditions.

Supplementary Note S2. Light projection analysis for the probe

According to the definition of the numerical aperture of an optic lens

$$NA = n\sin\theta \quad \text{(S1)}$$

Where n is the refractive index of the material and θ is the angle of acceptance. Then, we can get

$$\theta = \arcsin\left(\frac{NA}{n}\right) \quad \text{(S2)}$$

Table. S1 Material parameters of the optical fibers

Fiber type	Diameter	Material	Numerical aperture	Refractive index
Fiber bundle	450 (μm)	PMMA plastic	0.5	1.49
Light guide fiber	125 (μm)	Quartz glass	0.22	1.46

Based on the material parameters of the optical fiber shown in Table S1, the angle of acceptance for the light guide fiber θ_1 and the fiber bundle θ_2 can be calculated as follows.

$$\theta_1 = \arcsin\left(\frac{0.22}{1.46}\right) = 0.1513\text{rad} = 8.67\,\text{deg} \quad \text{(S3)}$$

$$\theta_2 = \arcsin\left(\frac{0.5}{1.49}\right) = 0.3419\text{rad} = 19.59\,\text{deg} \quad \text{(S4)}$$

Besides, according to the definition of the angle of divergence for an optical fiber $\gamma = \arcsin(NA)$, we can obtain the corresponding angle of the light guide fiber

$$\gamma_1 = \arcsin 0.22 = 0.2218\text{rad} = 12.71\text{deg} \text{ (S5)}$$

Based on the above calculations, we can further obtain the projection radius of the fiber array on a reflective board with a distance of *ds* from the tip plane of the probe.

$$R_1 = \frac{d_1}{2} + ds \sin \gamma_1 \text{ (S6)}$$

$$R_2 = \frac{d_2}{2} + ds \sin \theta_2 \text{ (S7)}$$

And the corresponding projection areas are

$$A_{lighting} = \pi R_1^2 \text{ (S8)}$$

$$A_{img} = \pi R_2^2 \text{ (S9)}$$

Given a far enough distance *ds*, the projection areas from each light guide fiber will intersect sufficiently and be smaller than the theoretical imaging area, shown as Fig. S4a. The gray region and the central white region correspondingly represents the fiber bundle projection and the effective imaging area. The blue region denotes the difference between the effective imaging area and the virtual imaging zone. And the region labeled by yellow represents the $1/n_f$ part of the effective imaging area. When there is only a single light guide fiber, the effective imaging area is πR_1^2. For the scenario of embedding more light guide fibers, the corresponding area can be represented as

$$A_{effect} = \sum_{n_f} 2(A_{S\_o_{11}AB} + A_{T\_o_{11}Bo2}), (n_f \in [2,6]) \text{ (S10)}$$

$$A_{S\_o_{11}AB} = \frac{1}{2} R_1^2 \alpha_{n_f} \text{ (S11)}$$

$$A_{T\_o_{11}Bo2} = \frac{d_1 + d_2}{4} R_1 \sin(\pi - \alpha_{n_f}) \text{ (S12)}$$

Where

$$\alpha_{n_f} = \begin{cases} \pi - \arccos \frac{o_{11}o_{12}}{2R_1}, n_f = 2 \\ \pi - \frac{\pi}{6} - \arccos \frac{o_{11}o_{12}}{2R_1}, n_f = 3 \\ \pi - \frac{\pi}{4} - \arccos \frac{o_{11}o_{12}}{2R_1}, n_f = 4 \\ \pi - \frac{3\pi}{10} - \arccos \frac{o_{11}o_{12}}{2R_1}, n_f = 5 \\ \pi - \frac{\pi}{3} - \arccos \frac{o_{11}o_{12}}{2R_1}, n_f = 6 \end{cases} \text{ (S13)}$$

$$o_{11}o_{12}=\begin{cases} d_1+d_2, n_f=2 \\ \frac{\sqrt{3}}{2}(d_1+d_2), n_f=3 \\ \frac{\sqrt{2}}{2}(d_1+d_2), n_f=4 \\ (d_1+d_2)\sin\frac{\pi}{5}, n_f=5 \\ (d_1+d_2)\sin\frac{\pi}{6}, n_f=6 \end{cases} \quad \text{(S14)}$$

Then, we can calculate the theoretical value of the effective imaging area A_{effect}. And the projection ratio of light covering area over the imaging region can be obtained as

$$ra_{proj}=\frac{A_{effect}}{A_{img}} \quad \text{(S15)}$$

To further verify the variation trend, we find that the effective imaging zone becomes more likely a circle (virtual imaging zone) with a radius of R_{vir} as the increasing of light guide fibers. Where

$$R_{vir}=R_1+\frac{d_1+d_2}{2} \quad \text{(S16)}$$

Take the distance $ds=4.5$ mm as an example, the calculated effective imaging area and the difference with the virtual zone can be seen in Fig. S4b. With the increase of light guide fiber number, the effective imaging area (the colored bar) gets more close to the virtual imaging zone A_{vir} (the black dashed line). And the relative difference decrease from ~38% to ~3% as the light guide fibers increases from one to six.

Supplementary Note S3. Mechanical analysis for the skeleton

According to the definition of axial stress, it means the normal force F_N loaded on a unit area of the cross-section.

$$\sigma_{normal}=\frac{F_N}{A} \quad \text{(S17)}$$

where $A=\frac{\pi}{4}\left(D_0^2-d^2-(i+1)d_h^2\right), i\in[1,6]$ denotes the area of the skeleton with different hollow structures and D_o, d_o, and d_h represent the diameter of the outer/inner contour and the peripheral hole, respectively (Fig. S6a). As for the bending stress caused by a lateral load F_s, it can be expressed as

$$\sigma_{lateral}=\frac{M}{I_x}=\frac{F_s l}{I_x} \quad \text{(S18)}$$

where l and I_x denote the length between the load point and the fixed support and the area moment of inertia, respectively. And the inertia can be calculated according to $I_x = \int y^2 dA$, where y denotes the distance between any unit area dA and the Y axis. Besides, the torsional stress of the skeleton can be represented by the loaded torque T

$$\tau_{torque} = \frac{T}{I_p} \text{(S19)}$$

Where I_P denotes the polar moment of inertia and can be computed by $I_p = \int \rho^2 dA$, where ρ denotes the polar distance between any unit area dA and the polar origin.

The structural dimension of the designed skeleton and the corresponding mechanical parameters of the utilized material for the micro 3D printing can be found in Table S2 and Table S3, respectively.

Table. S2 Structural dimension of the skeleton

Name	D_o	d_o	d_h	d	h	l
(μm)	750	460	130	600	80	3000

Table. S3 Material parameters of the printed skeleton

Material	Elastic modulus (GPa)	Tensile strength (MPa)	Bending strength (MPa)
HTL	4.2	79.3	120

As the HTL belongs to plastic materials, the torsional strength is usually viewed as about half of the tensile strength, i.e., $[\tau] = (0.5 \sim 0.6)[\sigma_{ten}]$. Here, the torsional strength is defined as $[\tau] = 0.55[\sigma_{ten}] = 43.615\,\text{MPa}$.

Based on the structure dimensions, we have established the 3D models for the six skeletons with diverse hollow structures by using the software SolidWorks 2016. The top view of the six skeletons can be seen shown in Fig. S5a. According to the materials parameters, we carried out the mechanical analysis with series of simulations in software ANSYS 2021, the corresponding simulation results under normal loading, lateral loading, and torque loading can be found in Fig. S5b, c, d, respectively.

As stated in the materials and methods section, to address the challenges posed by the low strength and printing difficulties associated with the ultrathin fillets connecting the peripheral holes to the central lumen, we have modified the design by resecting these fillets into parallel planes.

To verify the necessity of the structural modification, we compared the mechanical performance of a skeleton with four peripheral holes with/without such resection.

As shown in Fig. S6b, the original thickness of the fillets is only 5 μm, resulting in low strength and fabrication difficulties. To improve the mechanical performance, we modified the skeleton structure by resecting the original ultrathin fillets into parallel-plane types with an 80 μm width (Fig. S6a). As the simulation results shown in Fig. S7, the modified skeleton structure shows a much better mechanical performance than the

original one when subjecting the same normal/lateral/torsional load.
According to the FEM results shown in Fig. 2i/j/k, the modified skeleton structure would reach the strength limit under a normal/lateral/torsional load of about 15.7 N, 1.2 N, and 0.35 N/mm, respectively, which greatly exceeds the subjected load in clinical practice. Thus, the skeleton structure would not meet failure.

Supplementary Note S4. Friction test of the elastomer with/without hydrogel formation

To assess the friction-reducing performance of the hydrogel skin generated on the outer surface of the continuum robot, we carried out corresponding measurements. As shown in Fig. S8a, we prepared two pieces of pure elastomer, including the translucent one reserving as the substrate for sliding tests and the red one as the sample. To ensure the single variable condition, we evenly divided the red elastomer into four parts. Two samples (3,4) are selected for generating the hydrogel skin while the rest two (1,2) keeping unprocessed state.
The experimental setup for testing the sliding frictions is shown in Fig. S8b. Here, the sample is placed on the top of the substrate, connected with the fixed forcemeter through a connection wire. The substrate is fixed on the moving platform of the screw motor module below. With the platform moving in the direction away from the forcemeter, the induced sliding friction between the samples and the substrate can then be measured and recorded.
Fig. S8c shows the measured pulling force variation of the four samples under dry/wet environments. Apparently, the samples with hydrogel skin cause smaller pulling force compared with the bare samples, e.g., the maximum value of the bared ones are larger than 1.5 N while that of the gelled less than 0.2 N. It suggests a smaller sliding friction induced between the hydrogel-formed samples and the substrate. Besides, it can also be concluded that, for the bare samples, the dry contact condition induces larger friction than the wet. To further verify the similar trend of the gelled samples, we have loaded a 100 grams weight on the top. The corresponding testing results can be seen in Fig. S8d. The dry contact condition induces a maximum pulling force ~4.0 N while that of the wet smaller than 1.0 N.
The series of friction tests on the one hand prove the lubrication effect of the hydrogel skin formation, e.g., reducing the friction of 8/20 folds under dry/wet conditions at least, respectively. On the other hand, it suggests that the gelled skin will show more obvious lubrication performance under a wet contact, paving the application potential in accessing channel environments in the human body.

Supplementary Note S5. Light intensity transmission analysis for the probe

The theoretical transmitted light flux from the light guide fiber can be expressed as

$$\Phi_{tran} = \int_0^{\frac{d_1}{2}} I_{(r)} 2\pi r dr \approx \int_0^{\infty} I_o e^{\frac{-2r^2}{w_0^2}} 2\pi r dr = \frac{\pi}{2} w_0^2 I_o \quad \text{(S20)}$$

Where I_o denotes the maximum intensity on the virtual fiber tip when $r = 0$, and w_o

represents the radius of the light projection, i.e., the Gaussian radius. Here, the radius can be approximated to be 25.2 μm. For the receiving plane of the detector tip, with a distance 2*ds* from the virtual fiber tip, the diameter of the cross-sectional plane of the light flux is $D = d_1 + 4ds\tan(\gamma_1)$. And the new Gaussian radius used to characterize the light intensity distribution profile changes into $w = 2ds\tan(\gamma_1) + w_o$. Then, the above equation can also be represented as

$$\Phi_{tran} = \int_0^{\frac{D}{2}} I_{(r)} 2\pi r dr \approx \int_0^{\infty} I'_o e^{\frac{-2r^2}{w^2}} 2\pi r dr = \frac{\pi}{2} w^2 I'_o \text{(S21)}$$

Where I'_o denotes the maximum intensity on the receiving fiber tip when $r = 0$, and the corresponding value can be computed as $I'_o = \left(w_0 / w\right)^2 I_o$.

As the real light flux is distributed in the three-dimensional space, like a cone shape, the collected light flux from the central fiber bundle tip will be an irregular and incomplete cylinder. Then, the collected light flux should be calculated according to the following integral.

$$\Phi_{col} = \iint I'_o e^{\frac{-2(x^2+y^2)}{w^2}} dydx \text{(S22)}$$

As shown in Fig.3b, given a reflective board placed with an offset *dr* to the central plane of the probe, the collected light flux from the second and the third light guide fiber will be always the same. Based on the coordinate system, the theoretical reflected/collected light flux from the three light guide fibers can be calculated according to the following equations.

For the reflected light flux, it is only affected by the position of the reflective board. Thus, the range along the y-axis can be expressed as

$$\begin{cases} y_{R1} \in [-D/2, dr - \left(d_1 + d_2\right)/2] \\ y_{R2} \in [-D/2, dr + \left(d_1 + d_2\right)/2 * \sin\left(\pi/6\right)] \\ y_{R3} \in [-D/2, dr + \left(d_1 + d_2\right)/2 * \sin\left(\pi/6\right)] \end{cases} \text{(S23)}$$

Then, the corresponding integral range along the x-axis can be further represented as

$$x_{Ri} \in [-\sqrt{D^2/4 - y_{Ri}^2}, \sqrt{D^2/4 - y_{Ri}^2}], i = 1,2,3 \text{ (S24)}$$

Thus, the theoretical reflected light from each light guide fiber is

$$\Phi_{tran\_i} = \int_{x_{Ri\min}}^{x_{Ri\max}} \int_{y_{Ri\min}}^{y_{Ri\max}} I'_o e^{\frac{-2(x^2+y^2)}{w^2}} dydx, i = 1,2,3 \text{ (S25)}$$

And the total reflected flux can be obtained as

$$\begin{aligned}\Phi_{tran\_total} &= \Phi_{tran\_1} + \Phi_{tran\_2} + \Phi_{tran\_3} \\ &= \Phi_{tran\_1} + 2\Phi_{tran\_2}\end{aligned} \quad \text{(S26)}$$

The calculated reflected flux against both the distance *ds* and the offset *dr* from the first/second/total light guide fibers can be found in Fig. S10a, b, and c, respectively. For the first light guide fiber, the reflected flux shows two different trends, e.g., increasing as the distance increases when the offset is smaller than 0.225 mm while decreasing with distance increasing for a bigger one. Similarly, the reflected flux from the second light guide fiber shows two types of changing trends but the offset threshold is -0.2 mm. The total reflected flux presents four trends, e.g., keep increasing, decreasing first and increasing later, increasing first and decreasing later, and keep decreasing.

For the collected flux from each light guide fiber, it will be affected by both the position of the reflective board and the radius of the central fiber bundle. When the offset of the board is within the diameter range of the fiber bundle, i.e., $-d_2/2 < dr < d_2/2$, the range along the y-axis can be expressed as

$$\begin{cases} y_{C1} \in [-D/2, dr - (d_1 + d_2)/2], D < d_1 + 2d_2 \\ y_{C1} \in [-d_1/2 - d_2, dr - (d_1 + d_2)/2], D \geq d_1 + 2d_2 \end{cases} \quad \text{(S27)}$$

$$y_{C2} \in [-d_2/2 + (d_1 + d_2)\sin(\pi/6)/2, dr + (d_1 + d_2)\sin(\pi/6)/2] \quad \text{(S28)}$$

When the offset of the board is higher than the radius of the fiber bundle, i.e., $dr \geq d_2/2$, the range along the y-axis can be changed into

$$\begin{cases} y_{C1} \in [-D/2, -d_1/2], D < d_1 + 2d_2 \\ y_{C1} \in [-d_1/2 - d_2, -d_1/2], D \geq d_1 + 2d_2 \end{cases} \quad \text{(S29)}$$

$$\begin{cases} y_{C2} \in [-d_2/2 + (d_1 + d_2)\sin(\pi/6)/2, D/2], D < d_2 + (d_2 + d_2)\sin(\pi/6) \\ y_{C2} \in [-d_2/2 + (d_1 + d_2)\sin(\pi/6)/2, d_2/2 + (d_1 + d_2)\sin(\pi/6)/2], \\ \quad D \geq d_2 + (d_2 + d_2)\sin(\pi/6) \end{cases} \quad \text{(S30)}$$

Besides, for the scenario that the reflective board is lower than the radius of the fiber bundle, i.e., $dr < -d_2/2$, there would be no flux collected by the central fiber bundle theoretically, i.e., $\Phi_{col\_total} = 0$.

Further, the corresponding integral range along the x-axis can be represented as

$$\begin{cases} x_{C1} \in [-\sqrt{d_2^2/4 - (y_{C1} + d_1/2 + d_2/2)^2}, \sqrt{d_2^2/4 - (y_{C1} + d_1/2 + d_2/2)^2}] \\ x_{C2} \in [-\sqrt{d_2^2/4 - (y_{C1} - (d_1 + d_1)\sin(\pi/6)/2)^2} + (d_1 + d_1)\cos(\pi/6)/2, \\ \quad \sqrt{d_2^2/4 - (y_{C1} - (d_1 + d_1)\sin(\pi/6)/2)^2} + (d_1 + d_1)\cos(\pi/6)/2] \end{cases} \quad \text{(S31)}$$

Thus, the theoretical collected light from each light guide fiber is

$$\Phi_{col\_i} = \int_{x_{Ci\min}}^{x_{Ci\max}} \int_{y_{Ci\min}}^{y_{Ci\max}} I_o' e^{\frac{-2(x^2+y^2)}{w^2}} dydx, i = 1,2,3 \text{ (S32)}$$

The calculated collected flux against both the distance *ds* and the offset *dr* from the first/second light guide fiber can be found in Fig. S10d, and e, respectively. All of them show a similar trend of first increasing and decreasing later with the increase of distance. Besides, the maximum keeps almost steady when the offset is larger than 0.225 mm. And the total collected flux can be obtained as

$$\begin{aligned} \Phi_{col\_total} &= \Phi_{col\_1} + \Phi_{col\_2} + \Phi_{col\_3} \\ &= \Phi_{col\_1} + 2\Phi_{col\_2} \end{aligned} \text{ (S33)}$$

Then the ratio of collected light flux over the reflected one is represented as

$$\Phi_{ratio} = \frac{\Phi_{col\_total}}{\Phi_{tran\_total}} \text{ (S34)}$$

The corresponding variation trend is shown in Fig. S10e. The ratio shows a trend of increasing first and decreasing later as increasing the distance. Moreover, the maximum ratio presents near the distance of ~1.0 mm.

Based on the equation (S26), the theoretical intensity distribution profile from the light guide fibers can also be calculated. Fig. S11a and b show the distribution and the corresponding contour map at a distance of 1.0 mm, respectively. Given a fiber bundle in the center and a reflective board with offset *dr*, as shown in Fig. S11b, the collected light intensity from the four quadrants can be calculated. For the distance of 1.0 mm, the normalized value of the collected intensity from the top right and bottom right quadrants can be shown in Fig. S11c. When the offset *dr* is smaller than -0.2 mm, there is no light collected by the central fiber bundle and the normalized intensities are equal to zero. When the offset is between -0.2 mm and 0.1 mm, the normalized intensity from the BR quadrant is 0.5 due to no light collected by upper two quadrants. However, as the offset further increases, the normalized intensity from the BR quadrant decreases and that of the TR increases. Both of them finally equal to 0.25 when the offset *dr* is larger than 0.225 mm.

According to equation (S33), we can further obtain the collected flux from the four quadrants against distance under diverse offset. The variation from the TR and BR region can be found in Fig. S11d, and e, respectively. Then, the changing trend of the normalized intensity from both the BR and TR quadrants against distance *ds* under diverse offset *dr* can be calculated and presented in Fig. S11f. For an offset between -0.2 mm and 0 mm, the normalized intensities from TR and BR quadrants are respectively always 0 and 0.5 despite the distance. Given the offset between 0 mm and 0.225 mm, the normalized intensities from TR and BR quadrants correspondingly show increasing and decreasing trend while keep almost constant for a distance larger than 1.0 mm, e.g., BR holds 0.322 and 0.255 for the offset of 0.1 mm and 0.2 mm, respectively. When the offset is larger than 0.225 mm, the normalized intensities from the four quadrants show a similar trend with the former while the value after 1.0 mm distance becomes 0.25.

Based on the variation trend of both the collected intensities and the corresponding normalized values from the four quadrants, we can estimate the existence and the orientation of the reflective board respect to the probe tip, e.g., a quadrant with a normalized intensity bigger than 0.25 means the orientation of the obstacle in front. Similarly, we can utilize the experimental recorded intensity data to estimate the obstacle in front therefore achieve safe navigation inside the channel environment.

Supplementary Note S6. Imaging performance of the probe

To investigate the imaging performance of the probe, we designed the corresponding experimental setup (Fig. S12). We first set a reflective board on the moving platform (the ball screw motor module) and fixed the probe on the top of a four degree-of-freedom (X-Y-Z-θ) adjustable base (Fig. S12a). As the experimental preparation, the base is utilized to achieve the probe tip plane be parallel to the reflective board and initial distance between them be zero. During the experiments, the moving platform is controlled to increase the distance *ds* after adjusting the lateral offset *dr* manually.
To study the imaging performance of recognizing an object and the resolution, we further fixed a calibration board on the top of the reflective board (Fig. S12b). Before the experiment, the adjustable base can be utilized to move the given pattern to the endoscopic view. With the distance *ds* changed by the ball-screw motor module, the object recognition performance can then be examined.

S6.1 Out-of-sight obstacle detection

Based on the experimental setup described in Fig. S12a, we obtain the intensity variation trend against distance *ds* under different lateral offset *dr*, as shown in Fig. 3d. Here, the measured intensity is represented by the sum of pixel intensity inside the view. To further investigate the out-of-sight detection strategy, the corresponding collected intensity and the normalized value from the four quadrants of the view under diverse offset have been presented in Fig. S13. Generally, the intensities from the four quadrants with different offset conditions all show a similar trend of first increase and later decrease as the distance increases. To find out the inherent intensity distribution error between the four quadrants induced by the experimental setup, we first set an obstacle in front that is large enough to fully cover the probe tip, the recorded intensities and the corresponding normalized value can be seen in Fig. S13a. Theoretically, there would be no intensity difference between the four quadrants and the normalized value shall be equal to 0.25 that can not be utilized to confirm the orientation, if facing a large enough obstacle. Here, the recorded difference can be viewed as the inherent error induced by the experimental setup. Besides, the normalized values are within the range of 0.17-0.33 despite the distance. Therefore, we set this range as the threshold that can not confirm the orientation of the obstacle in front.
With an offset smaller than 0 mm, the intensity difference between the four quadrants can be utilized to estimate the existence of an obstacle. However, the normalized value of the four quadrants are within the threshold range that can not determine the

orientation of the obstacle in front (Fig. S13b, c). For a bigger offset (0.0 mm to 0.5 mm), the intensity and the corresponding normalized value from the four quadrants show obvious difference and exceed the threshold, which can then be utilized to confirm the existence and orientation of the obstacle in front (Fig. S13d-i).

The statistical result of the out-of-sight obstacle detection performance against the lateral offset *dr* is shown in Fig. S14. The light orange region denotes the distance range under diverse offsets that can distinguish the orientation of the obstacle in front. Generally, the range is about 4.0 mm for different offset and ends farther as offset increasing, e.g., it ends at a distance of ~3.0 mm under 0.0 mm offset, ~5.8 mm under 0.2 mm offset, and ~9.4 mm under 0.5 mm offset. The results suggest that the proposed probe can achieve an obstacle detection distance up to ~9.4 mm, a tenfold improvement from the theoretical blur obstacle detection distance limit (~1.0 mm).

S6.2 Target recognition

To study the capacity of target imaging, we employed the experimental setup shown in Fig. S12b. To assess the target recognition performance, we first adopt a series of imaging processing procedures for segmenting the contour, as shown in Fig. S16. During the experiments, we found that the recognition performance is not only affected by the distance but also the exposure durations of the camera. According to Fig. S17, with difference exposure durations set, the symbol can be clearly/obscurely recognized within diverse distance range, e.g., setting an exposure duration of 30 ms, the object can be clearly/obscurely recognized within the distance range of 0.07/0.139 mm, and the corresponding distance range are 0.143/0.223 mm for the exposure duration of 10 ms. Under diverse exposure conditions, the collected flux intensity and the statistical results of recognizing object can be seen in Fig. S17a, and b, respectively. It suggests the imaging performance under 10 ms exposure duration is the best among the conditions of 5 ms to 30 ms. To verify the superiority of 10 ms exposure duration, we further compare the recognition performance of diverse exposure conditions at the specific distance of 0.143/0.223 mm, as shown in Fig. S17. It can be concluded that, at the clear recognition threshold of 0.143 mm, the segmented contour with 10 ms exposure condition shows more features and is more alike the given number symbol “5”. As for the obscure recognition threshold of 0.223 mm, the extracted contour from 10 ms group also shows more features that similar to a hook, the symbol “5” without a horizontal line.

Except for the object recognition performance, we also investigate the imaging resolution of the proposed endoscopic system. Here, we employ the standard calibration bars from the fourth group test chart of the USAF 1951 as the testing object. The results can be seen in Fig. S19. With a 24.8 μm for both the width of the standard bars and the distance between them, the captured images show thinner bars as the exposure durations increasing, e.g, the width decreases from ~23 μm for 5 ms to ~12.5 μm for 30 ms. The corresponding capture error increases from ~7% (~2 μm) for 5 ms to ~50% (~12.5 μm) for 30 ms, shown as Fig. S20c.

In short, the proposed probe and the corresponding endoscopic imaging system can

achieve competitive imaging performance for microscale object, e.g., setting the exposure duration of the camera as 10 ms, we can achieve a better contour segmentation within a long distance and the capture error low to ~2.0 μm for the target. The performed imaging resolution surpasses that of most clinically used endoscopes, which typically with a resolution of about 10 μm (cellular/subcellular resolution)[14,15]. Besides, to improve the captured image contrast, we can either set a proper exposure parameter or optimize the image processing algorithms. In the future work, we plan to develop a system that includes an automatic adjustment algorithm for exposure duration and image processing procedures to advance the clinical application of our proposed fiberscopic robot.

Supplementary Note S7. Light intensity distribution-based environment exploration strategy

To achieve effective and safe steering, the exploration ability in a farther region than the maximum imaging distance (1mm) is essentially significant for identifying the branches and obstacles to make proper decisions (e.g., entrance or bypass) in advance. To address this challenge, we proposed an intensity distribution-based environment exploration strategy and extended the blur obstacle detection distance approximately 10 folds farther to ~9.4 mm, shown in Fig. 3f.

Employing the proposed strategy, we further proposed a flowchart for implementing the interventional surgery procedure safely (Fig. S22). At the beginning of accessing certain channel environment, e.g., the lung bronchia tree channel, the sheath with probe integrated is advanced by the back-end advancing platform. Through monitoring the collected intensity, we can primarily predict there is an obstacle in front when the value shows an increasing trend, or a free channel for a constant low intensity. Based on the prediction of an obstacle in front, with further analyzing the normalized intensities from the four quadrants as exceeding the threshold or not, we can confirm the orientation of the obstacle as towards certain direction or straight ahead. After confirming the orientation of the obstacle, we can choose to steer the sheath/probe towards darker/brighter region for avoiding/approaching the obstacle. An increasing trend can be observed during the approaching process, and the probe will then be advanced closer to the obstacle and achieve in situ imaging. According to the captured images, we can know that if there is a pathological area found. And a further in situ treatment can be implemented on the pathological tissue if necessary. Finally, the sheath and probe shall be retrieved and leave the channel environment.

Supplementary Note S8. Deformation analysis of the continuum robot under multi-sectional magnetic actuation

As depicted in Fig. 4a, the continuum robot consists of the soft sheath with magnetic tip and the submillimeter probe coated with magnetic skin. A permanent magnet is employed to actuate the magnetic sheath for achieving coarse steering during the interventional process. And a three-degree-of-freedom electromagnetic Helmholtz coil

system is later utilized to precisely control the motion of the magnetic probe for in situ surgical manipulations.

S8.1 Deformation model of the magnetic sheath under gradient magnetic field

When the magnetic sheath is placed inside the gradient magnetic field generated by the permanent magnet, an induced magnetization along its axial direction will be immediately generated inside the magnetic polymer, which subjects the sheath to both the magnetic force $\mathbf{F}_{msh}$ and magnetic torque $\mathbf{T}_{msh}$, as shown in Fig. S23a. Among them, the force will cause the sheath tip move from the space with sparse magnetic field to intensive area, towards the magnet. Besides, the torque will bend the sheath tip to parallel with the virtual magnetic field curve nearby. Define the induced magnetization of an infinite volume unit as vector $\mathbf{m}_{sh}$, we can obtain the whole magnetization for the magnetic section as

$$\mathbf{M}_{sh} = \int \mathbf{m}_{sh} A_{msh} ds = \mathbf{m}_{sh} A_{msh} L_{msh} \text{ (S35)}$$

Where A_{msh} and L_{msh} denote the cross-section area and the length of the magnetic skin on the probe tip. Given a magnetic field $\mathbf{B}_{sh} = \begin{bmatrix} B_{shx} & B_{shy} & B_{shz} \end{bmatrix}^{\mathrm{T}}$ applied to the magnetic sheath, the corresponding magnetic force $\mathbf{F}_{msh}$ and magnetic torque $\mathbf{T}_{msh}$ can be expressed as

$$\mathbf{F}_{msh} = (\mathbf{M}_{sh} \cdot \nabla)\mathbf{B}_{sh} \text{ (S36)}$$

$$\mathbf{T}_{msh} = \mathbf{M}_{sh} \times \mathbf{B}_{sh} \text{ (S37)}$$

Where ∇ is a gradient operator. Considering the length between the magnetic section and the whole probe $L_{msh} << L_{sh}$, we can correspondingly simplify the accumulated magnetic force and magnetic torque from this section as a point magnetic force and total magnetic torque applied to the distal tip of the probe. Then, we can obtain the equilibrium equation of the magnetic sheath as

$$EI \frac{d\eta_{sh}}{dl_{sh}} = -T_{msh} - F_{msh}\left(L_{sh} - l_{sh}\right) + \int_{l_{sh}}^{L_{sh}} -g_{sh} A_{sh} (L_{sh} - l_{sh}) \sin(\eta_{sh}) dl_{sh}, l_{sh} \in (0, L_{sh}) \text{ (S38)}$$

To further simplify the above piecewise equilibrium equations, we utilize the superposition method of beam deformation to calculate the sheath tip's deformation and bending angle due to the small deformation condition. We assume the proposed sheath' deformation as the combined results of the magnetic-induced deformation of a sheath coated with magnetic skin on the distal tip with an infinitesimal length (Fig. S23b) and the gravity-induced deformation of a probe without magnetic skin (Fig. S23c), i.e., $\delta_{sh\_all} = \delta_{sh1} + \delta_{sh2}$ and $\eta_{sh\_all} = \eta_{sh1} + \eta_{sh2}$. The corresponding equilibrium equations for the three virtual probes can be expressed as

$$EI\frac{d\eta_{sh}}{dl_{sh}} = -T_{msh} - F_{msh}\left(L_{sh} - l_{sh}\right), l_{sh} \in (0, L_{sh}) \text{ (S39)}$$

$$EI\frac{d\eta_{sh}}{dl_{sh}} = \int_{l_{sh}}^{L_{sh}} -g_{sh}A_{sh}(L_{sh} - l_{sh})\sin(\eta_{sh})dl_{sh}, l_{sh} \in (0, L_{sh}) \text{ (S40)}$$

Integrating both sides of equation S39 from 0 to L_{sh} yields

$$EI\eta_{sh} = -T_{msh}l_{sh} + \frac{1}{2}F_{msh}\left(L_{sh} - l_{sh}\right)^2 + C1, l_{sh} \in (0, L_{sh}) \text{ (S41)}$$

The constants C1 can be determined from the boundary condition that there is no bending angle at the corresponding fixation, i.e., $\eta_{sh}(0) = 0$, which leads to

$$C1 = -\frac{1}{2}F_{msh}L_{sh}{}^2 \text{ (S42)}$$

Then, equation S41 can be written as

$$EI\eta_{sh} = -T_{msh}l_{sh} + \frac{1}{2}F_{msh}\left(L_{sh} - l_{sh}\right)^2 - \frac{1}{2}F_{msh}L_{sh}^2, l_{sh} \in (0, L_{sh}) \text{ (S43)}$$

Substituting $l_{sh} = L_{sh}$ into equation S43, we can obtain the tip's bending angle caused by magnetic field as

$$\eta_{sh1} = \frac{-1}{EI}\left(T_{msh}L_{sh} + \frac{1}{2}F_{msh}L_{sh}^2\right) \text{ (S44)}$$

Further integrating both sides of equation S43 yields

$$EI\omega_{sh} = -\frac{1}{2}T_{msh}l_{sh}^2 - \frac{1}{6}F_{msh}\left(L_{sh} - l_{sh}\right)^3 - \frac{1}{2}F_{msh}L_{sh}^2 l_{sh} + D1, l_{sh} \in (0, L_{sh}) \text{ (S45)}$$

The constants D1 can be determined from the boundary condition that there is no deflection at the corresponding fixation, i.e., $\omega_{sh}(0) = 0$, which leads to

$$D = \frac{1}{6}F_{msh}L_{sh}{}^3 \text{ (S46)}$$

Then, equation S45 can be written as

$$EI\omega_{sh} = -\frac{1}{2}T_{msh}l_{sh}^2 - \frac{1}{6}F_{msh}\left(L_{sh} - l_{sh}\right)^3 - \frac{1}{2}F_{msh}L_{sh}^2 l_{sh} + \frac{1}{6}F_{msh}L_{sh}{}^3, l_{sh} \in (0, L_{sh}) \text{ (S46)}$$

Substituting $l_{sh} = L_{sh}$ into equation S46, we can obtain the tip's deflection caused by magnetic field as

$$\delta_{sh1} = \frac{-1}{EI}\left(\frac{1}{2}T_{msh}L_{sh}^2 + \frac{1}{3}F_{msh}L_{sh}^3\right) \text{ (S47)}$$

Differentiating both sides of equations S40, we can get

$$EI\frac{d^2\eta_{sh}}{dl_{sh}^2} = -g_{sh}A_{sh}(L_{sh} - l_{sh})\sin(\eta_{sh}), l_{sh} \in (0, L_{sh}) \text{ (S48)}$$

Multiplying both sides with a $d\eta_{de}$ and integrating them yields

$$\int EI\frac{d^2\eta_{sh}}{dl_{sh}^2}\frac{d\eta_{sh}}{dl_{sh}}dl_{sh}=\int -g_{sh}A_{sh}(L_{sh}-l_{sh})\sin(\eta_{sh})d\eta_{sh}, l_{sh}\in(0,L_{sh}) \text{ (S49)}$$

Then, we can get the following form

$$\frac{1}{2}EI\left(\frac{d\eta_{sh}}{dl_{sh}}\right)^2=g_{sh}A_{sh}(L_{sh}-l_{sh})\cos(\eta_{sh})+C2, l_{sh}\in(0,L_{sh}) \text{ (S50)}$$

The constants C2 can be determined from the boundary condition that there is no bending moment at the corresponding distal tip, i.e., $\eta'_{sh}(L_{sh})=0$, which leads to

$$C2=0 \text{ (S51)}$$

Then we can obtain

$$\sqrt{L_{sh}-l_{sh}}dl_{sh}=\sqrt{\frac{EI}{2g_{sh}A_{sh}}}\frac{d\eta_{sh}}{\sqrt{\cos(\eta_{sh})}}, \eta_{sh}\in(0,\eta_{sh2}) \text{ (S52)}$$

Integrating both sides yields

$$\frac{2}{3}L_{sh}^{\frac{3}{2}}=\sqrt{\frac{EI}{2g_{sh}A_{sh}}}\int_0^{\eta_{sh2}}\frac{d\eta_{sh}}{\sqrt{\cos(\eta_{sh})}}=f(\eta_{sh2}) \text{ (S53)}$$

Therefore, the bending angle η_{sh2} can be solved from equations S53. And we can obtain the total bending angle of the sheath as $\eta_{sh\_all}=\eta_{sh1}+\eta_{sh2}$.

Based on the relation of the infinitesimal arc length as

$$d\delta_{sh}=\sin(\eta_{sh})dl_{sh} \text{ (S60)}$$

Rearranging equation S52 as $dl_{sh}=f(\eta_{sh})d\eta_{sh}$, then integrating the above equation S60 yields

$$\delta_{sh2}=\int_0^{L_{sh}}\sin(\eta_{sh})dl_{sh}=\int_0^{\eta_{sh2}}f(\eta_{sh})\sin(\eta_{sh})d\eta_{sh} \text{ (S61)}$$

Therefore, the deflection of the sheath tip can then be obtained as

$$\delta_{sh\_all}=\delta_{sh1}+\delta_{sh2} \text{ (S62)}$$

S8.2 Deformation model of the magnetic probe under uniform magnetic field

The probe coated with magnetic skin in its distal end will bear magnetic torque $\mathbf{T}_{mde}$ when locating within the central workspace of the Helmholtz coil system. Define the generated uniform magnetic field within the x-o-y plane and at an angle φ_{de} with respect to the positive direction of the x-axis (i.e., $\mathbf{B}_{de}=\left[B_{de}\cos\varphi_{de}, B_{de}\sin\varphi_{de}\right]$). Taking the

infinite volume unit as an example, the induced magnetization within the unit can be denoted as vector $\mathbf{m}_{de}$, along the axial direction. Then, the whole magnetization for the magnetic section can be expressed as

$$\mathbf{M}_{de} = \int \mathbf{m}_{de} A_{mde} ds = \mathbf{m}_{de} A_{mde} L_{mde} \text{ (S63)}$$

Where A_{mde} and L_{mde} denote the cross-section area and the length of the magnetic skin on the probe tip. We can obtain the total magnetic torque T_{mde} as

$$T_{mde} = \left|\mathbf{M}_{de} \times \mathbf{B}_{de}\right| = m_{de} A_{mde} L_{mde} B_{de} \sin(\frac{\pi}{2} - \eta_{de}) = \tau_{mde} A_{mde} L_{mde} \text{ (S64)}$$

Except for the magnetic torque τ_{mde}, the gravity g_{de} is another force that the volume unit is subjected from the external environment (Fig. S24a). Here, the gravity g_{de} is simplified as constant for the entire probe. Then, for an arbitrary point P on the probe that is at an arc distance l_{de} with the proximal fixation and with an angle η_{de} between the tangent to the curve and the reference direction (i.e., negative direction of z-axis), we can obtain the equilibrium equation

$$EI\frac{d\eta_{de}}{dl_{de}} = \begin{cases} -\int_{l_{de}}^{L_{de}} \tau_{mde} A_{mde} dl_{de} + \int_{l_{de}}^{L_{de}} -g_{de} A_{de} (L_{de} - l_{de}) \sin(\eta_{de}) dl_{de}, l_{de} \in (L_{de} - L_{mde}, L_{de}) \\ -\tau_{mde} A_{mde} L_{mde} + \int_{l_{de}}^{L_{de} - L_{mde}} -g_{de} A_{de} (L_{de} - l_{de}) \sin(\eta_{de}) dl_{de}, l_{de} \in (0, L_{de} - L_{mde}) \end{cases} \text{ (S65)}$$

Where L_{de} and A_{de} represent the length and the cross-section area of the probe. To simplify the above piecewise equilibrium equations, we utilize the superposition method of beam deformation to calculate the tip's deformation and bending angle due to the small deformation condition. We assume the proposed probe' deformation as the combined results of the magnetic-induced deformation of a probe coated with magnetic skin on the whole body (Fig. S24b), the magnetic-induced deformation a probe with a magnetic skin length of $L_{de} - L_{mde}$ (Fig. S24c), and the gravity-induced deformation of a probe without magnetic skin (Fig. S24d), i.e., $\delta_{de\_all} = \delta_{de1} + \delta_{de2} + \delta_{de3}$ and $\eta_{de\_all} = \eta_{de1} + \eta_{de2} + \eta_{de3}$. The corresponding equilibrium equations for the three virtual probes can be expressed as

$$EI\frac{d\eta_{de}}{dl_{de}} = -\int_{l_{de}}^{L_{de}} \tau_{mde} A_{mde} dl_{de}, l_{de} \in (0, L_{de}) \text{ (S66)}$$

$$EI\frac{d\eta_{de}}{dl_{de}} = \int_{l_{de}}^{L_{de} - L_{mde}} \tau_{mde} A_{mde} dl_{de}, l_{de} \in (0, L_{de} - L_{mde}) \text{ (S67)}$$

$$EI\frac{d\eta_{de}}{dl_{de}} = \int_{l_{de}}^{L_{de}} -g_{de} A_{de} (L_{de} - l_{de}) \sin(\eta_{de}) dl_{de}, l_{de} \in (0, L_{de}) \text{ (S68)}$$

Differentiating both sides of equations S66 to S68, we can get

$$EI\frac{d^2\eta_{de}}{dl_{de}^2} = -m_{de} A_{mde} B_{de} \cos(\eta_{de}), l_{de} \in (0, L_{de}) \text{ (S69)}$$

$$EI\frac{d^2\eta_{de}}{dl_{de}^2}=m_{de}A_{mde}B_{de}\cos(\eta_{de}),l_{de}\in(0,L_{de}-L_{mde})\ (S70)$$

$$EI\frac{d^2\eta_{de}}{dl_{de}^2}=-g_{de}A_{de}(L_{de}-l_{de})\sin(\eta_{de}),l_{de}\in(0,L_{de})\ (S71)$$

Multiplying both sides with a $d\eta_{de}$ and integrating them yields

$$\int EI\frac{d^2\eta_{de}}{dl_{de}^2}\frac{d\eta_{de}}{dl_{de}}dl_{de}=\int -m_{de}A_{mde}B_{de}\cos(\eta_{de})d\eta_{de},l_{de}\in(0,L_{de})\ (S72)$$

$$\int EI\frac{d^2\eta_{de}}{dl_{de}^2}\frac{d\eta_{de}}{dl_{de}}dl_{de}=\int m_{de}A_{mde}B_{de}\cos(\eta_{de})d\eta_{de},l_{de}\in(0,L_{de}-L_{mde})\ (S73)$$

$$\int EI\frac{d^2\eta_{de}}{dl_{de}^2}\frac{d\eta_{de}}{dl_{de}}dl_{de}=\int -g_{de}A_{de}(L_{de}-l_{de})\sin(\eta_{de})d\eta_{de},l_{de}\in(0,L_{de})\ (S74)$$

Then, we can get the following form

$$\frac{1}{2}EI\left(\frac{d\eta_{de}}{dl_{de}}\right)^2=-m_{de}A_{mde}B_{de}\sin(\eta_{de})+D1,l_{de}\in(0,L_{de})\ (S75)$$

$$\frac{1}{2}EI\left(\frac{d\eta_{de}}{dl_{de}}\right)^2=m_{de}A_{mde}B_{de}\sin(\eta_{de})+D2,l_{de}\in(0,L_{de}-L_{mde})\ (S76)$$

$$\frac{1}{2}EI\left(\frac{d\eta_{de}}{dl_{de}}\right)^2=g_{de}A_{de}(L_{de}-l_{de})\cos(\eta_{de})+D3,l_{de}\in(0,L_{de})\ (S77)$$

The constants C1, D2 and D3 can be determined from the boundary condition that there is no bending moment at the corresponding distal tip, i.e., $\eta'_{de}(L_{de})=0$ and $\eta'_{de}(L_{de}-L_{mde})=0$, which leads to

$$\begin{cases}D1=m_{de}A_{mde}B_{de}\sin(\eta_{de1})\\D2=-m_{de}A_{mde}B_{de}\sin(\eta_{de2})\\D3=0\end{cases}\ (S78)$$

Then we can obtain

$$\frac{dl_{de}}{d\eta_{de}}=\frac{1}{\sqrt{\frac{2}{EI}m_{de}A_{mde}B_{de}\left[\sin(\eta_{de1})-\sin(\eta_{de})\right]}},\eta_{de}\in(0,\eta_{de1})\ (S79)$$

$$\frac{dl_{de}}{d\eta_{de}}=\frac{1}{\sqrt{\frac{2}{EI}m_{de}A_{mde}B_{de}\left[\sin(\eta_{de})-\sin(\eta_{de2})\right]}},\eta_{de}\in(0,\eta_{de2})\ (S80)$$

$$\sqrt{L_{de}-l_{de}}dl_{de}=\sqrt{\frac{EI}{2g_{de}A_{de}}}\frac{d\eta_{de}}{\sqrt{\cos(\eta_{de})}},\eta_{de}\in(0,\eta_{de3})\ \text{(S81)}$$

Integrating both sides yields

$$L_{de}=\int_0^{\eta_{de1}}\frac{d\eta_{de}}{\sqrt{\frac{2}{EI}m_{de}A_{mde}B_{de}\left[\sin(\eta_{de1})-\sin(\eta_{de})\right]}}=f_1(\eta_{de1})\ \text{(S82)}$$

$$L_{de}-L_{mde}=\int_0^{\eta_{de2}}\frac{d\eta_{de}}{\sqrt{\frac{2}{EI}m_{de}A_{mde}B_{de}\left[\sin(\eta_{de})-\sin(\eta_{de2})\right]}}=f_2(\eta_{de2})\ \text{(S83)}$$

$$\frac{2}{3}L_{de}^{\frac{3}{2}}=\sqrt{\frac{EI}{2g_{de}A_{de}}}\int_0^{\eta_{de3}}\frac{d\eta_{de}}{\sqrt{\cos(\eta_{de})}}=f_3(\eta_{de3})\ \text{(S84)}$$

Therefore, the bending angle η_{de1}, η_{de2} and η_{de3} can be solved from equations S82 to S84, respectively. And we can obtain the total bending angle of the probe as $\eta_{de\_all}=\eta_{de1}+\eta_{de2}+\eta_{de3}$.

Based on relation of the infinitesimal arc length as

$$\begin{cases}d\delta_{de}=\sin(\eta_{de})dl_{de}\\ dz_{de}=\cos(\eta_{de})dl_{de}\end{cases}\ \text{(S85)}$$

Rearranging equation S79 to S81 as $dl_{de}=g_i(\eta_{sh})d\eta_{sh},(i=1,2,3)$, then integrating the above equation S85 yields

$$\begin{cases}\delta_{dei}=\int_0^{L_{de}}\sin(\eta_{de})dl_{de}=\int_0^{\eta_{dei}}g_i(\eta_{dei})\sin(\eta_{de})d\eta_{de},(i=1,3)\\ \delta_{de2}=\int_0^{L_{de}-L_{mde}}\sin(\eta_{de})dl_{de}+(L_{de}-L_{mde})\sin(\eta_{de2})\\ \quad=\int_0^{\eta_{de2}}g_2(\eta_{de2})\sin(\eta_{de})d\eta_{de}+(L_{de}-L_{mde})\sin(\eta_{de2})\end{cases}\ \text{(S86)}$$

$$\begin{cases}z_{dei}=\int_0^{L_{de}}\cos(\eta_{de})dl_{de}=L_{de}-\int_0^{\eta_{dei}}g_i(\eta_{dei})\cos(\eta_{de})d\eta_{de},(i=1,3)\\ z_{de2}=\int_0^{L_{de}-L_{mde}}\cos(\eta_{de})dl_{de}+(L_{de}-L_{mde})\cos(\eta_{de2})\\ \quad=L_{de}-\int_0^{\eta_{de2}}g_2(\eta_{de2})\cos(\eta_{de})d\eta_{de}+(L_{de}-L_{mde})\sin(\eta_{de2})\end{cases}\ \text{(S87)}$$

Therefore, the coordinates of the probe tip can then be obtained as

$$\begin{cases}x_{de}=\delta_{de\_all}\cos(\varphi_{de})=(\delta_{de1}+\delta_{de2}+\delta_{de3})\cos(\varphi_{de})\\ y_{de}=\delta_{de\_all}\sin(\varphi_{de})=(\delta_{de1}+\delta_{de2}+\delta_{de3})\sin(\varphi_{de})\\ z_{de}=z_{de1}+z_{de2}+z_{de3}\end{cases}\ \text{(S88)}$$

Supplementary Note S9. Motion assessment of the continuum robot under multi-sectional magnetic actuation

S9.1 Motion assessment of the magnetic sheath actuated by gradient magnetic field

To assess the motion of the magnetic sheath actuated by gradient magnetic field, we carried out the corresponding characterization, as shown in Fig. S25. Given the soft sheath being fixed with diverse length L_{sh}, the deformation under magnetic actuation would be different. According to the deformation (Fig. S25a) and bending angle (Fig. S25b), we can conclude that the sheath with a shorter free beam length can be more difficult to actuated by the magnetic field, e.g., with a free length of 30 mm, the sheath tip generates a ~4 mm deformation and ~45 degree bending angle under magnetic field strength of ~68 mT while ~10 mm deformation and ~35 degree bending angle under ~37 mT for an 80 mm free beam. Besides, we obtain the root mean square error (RMSE) of the deformation and bending angle as ~0.25 mm and ~2.2 degree, respectively.

S9.2 Motion assessment of the magnetic probe actuated by uniform magnetic field

To assess the motion of the magnetic probe actuated by uniform magnetic field, we first design diverse linear trajectories, including the path along the x axis, y axis, and the diagonal direction. The obtained coordinates of the probe tip during the x-motion, y-motion, and diagonal motion from the vertical perspective recording system have been depicted in Fig S27a, b, and c, respectively. Compared with the designed paths, the probe has correspondingly achieved the root mean square error (RMSE) of about 16.5 μm, 16.5 μm, and 18.4 μm. The reconstructed trajectories in 3D space of the three types of linear motion can be seen in Fig. S27d. For the complex trajectories, e.g., square, circle, and spiral, the recorded coordinates of the probe tip have been depicted in Fig S28a, b, and c, respectively. And the error map has also been presented in Fig. S28d. The comprehensive RMSE of ~26 μm, ~22 μm, and ~27 μm can be calculated. Besides, with a peak to peak error of smaller than 100 μm, a planar object can be well kept within the imaging region, therefore successfully captured by the probe after approaching.

Supplementary Note S10. Interventional experiment inside an in vitro lung bronchial tree model

To demonstrate the magnetic navigation and imaging capacity of the proposed robotic system, we fabricated a 1:1 transparent bronchial tree model to carry out the interventional experiment. With a complex bifurcated channel environment and the inner diameter varies from 18 mm to 2.0 mm (Fig. S32), the bronchial model can be utilized to well verify the accessing ability of the continuum robot.

The results shown in Fig. 4i have demonstrate the capability of passing through tortuous channels with an inner diameter low to 2.0 mm and in situ scanning imaging for a grid pattern positioned at the distal tip of the channel. More data about the recorded intensity variation during the interventional process have been shown in Fig. S33. It can be

concluded that the key bifurcations inside the bronchial tree model can be successfully predicted.

Supplementary Note S11. In vitro experiments for demonstrating functional operations

Benefited from the functional channel embedded in the probe, various surgical tools can then be integrated to achieve corresponding surgical operations after reaching the pathological area. Here, we mainly demonstrate three types of operations in this manuscript, including sampling, drug delivery, and laser ablation. Before the ex vivo experiments shown in Fig. 5, we also carried out series of in vitro tests for validating their efficacy.

S11.1 In vitro liquid delivery experiment

To show the liquid delivery with the proposed continuum robot, we established the corresponding pumping subsystem and integrated it with the endoscopic imaging system, as shown in Fig. S34. Here, as the preliminary step of demonstrating drug delivery, the purified water is first employed as the delivering medium and a modified bauhinia flower pattern is utilized as the imaging target to verify the liquid delivery function under endoscopic imaging (Fig. S35a).

First, we filled 1 mL water into the syringe mounted on the injection pump. With the probe being manually positioned over the pattern, the pump is then started to automatic press the liquid into the sealed fluidic channel. At the meantime, the camera is activated to record the process after turning on the medical cold light in the endoscopic imaging system. The key moments of liquid delivery through the probe tip can be shown in the endoscopic snapshot (Fig. S35b). At the beginning (t0 s), both a star and a text symbol of "CITYU" have been captured while with a relatively low brightness. Then, within a duration of ~0.73 s, a brighter region quickly spreads from the top right direction to the entire view, which is actually the expansion of the fluidic contour. And the captured pattern can be recognized more clearly.

S11.2 In vitro laser delivery experiment

To show the laser delivery with the proposed continuum robot, we further established the corresponding laser subsystem and integrated it with the endoscopic imaging system, as shown in Fig. S36. Here, to preliminarily demonstrate laser ablation, a UV light is first employed as the laser source and a drop of UV responsive droplet below the modified bauhinia flower pattern is utilized as the irradiation target to verify the laser delivery function under endoscopic imaging (Fig. S37a).

During the experiment, a drop of UV responsive droplet is first dipped on a glass slide and positioned below the pattern with a distance *ds* of ~6.0 mm. With the probe being manually positioned over the pattern, the camera is activated to record the process after turning on the medical cold light in the endoscopic imaging system. Similarly, a star and a text symbol of "CITYU" have been captured at the beginning (Fig. S37b-1). Then,

turning on the UV light while shutting off the medical cold light, the endoscopic view suddenly becomes into bluish violet color and the pattern can be hardly recognized (Fig. S34b-2). After a UV duration of ~15 min, the droplet below the pattern is been examined under an optical microscope. A circular region (denoted by the dotted curve) located at the droplet center can be found with solidified block (Fig. S34b-4), which is obviously different with the fully fluidic status before the irradiation (Fig. S34b-3). The actual contour of the block with a diameter of ~2.86 mm has been shown in the inset.

S11.3 In vitro functional operations inside the printed bronchial tree model

To further validate the efficacy of the integrated functional operations of the proposed continuum robot, we have implemented an interventional experiment inside the printed lung bronchial tree model. The schematic of the liquid delivery and laser ablation at the distal end of the printed lung bronchial tree model can be seen in Fig. S28a.

As for the drug delivery test, 1 mL of water is first loaded into the syringe with a capacity of 5 mL. After the probe is navigated through the bifurcated channel under the magnetic actuation and finally reaches the glass plate, the grid pattern has been captured, as shown in Fig. S38b-2. Later, the syringe is controlled by the injection pump to deliver liquid into the sealed fluidic channel. Then, starting from the moment of t0 = 216 s, the fluidic contour is suddenly spread from the bottom to cover the whole endoscopic view within 0.4 s. When the probe is retrieved to completely leave the glass plate at t1 = 351.36 s, a drop of water can be clearly observed as adhering on the surface of the plate (Fig. S38b-3). With the examination under optical microscope, the droplet with a diameter of ~1.2 mm can be found, even showing the magnification effect for the grid pattern below (Fig. S38b-4, Supplementary Movie 3).

To demonstrate the laser ablation, a coiled of electrical tape with ~1.5 mm diameter is employed as the target positioned inside the end bronchus channel. After the probe is navigated through the bifurcated channel under the magnetic actuation and finally accesses the end bronchus channel, the near-infrared laser is turned on at t = 586.73 s (Fig. S38c-1). To better verify the NIL irradiation, we turned the medical cold light off and record the purplish red light transmitted from the probe tip at t = 586.76 s. With further advancing of the probe to approach the target, a purple region can be found in the endoscopic view at t = 679.84 s. After an irradiation duration of ~15 min, the NIL is then turned off. Finally, we check the sectional view of the coiled tape under optical microscope and find an obvious burning region with a diameter of ~470 μm with respect to the original one (Fig. S38c-2, Supplementary Movie 4).

Supplementary Figures

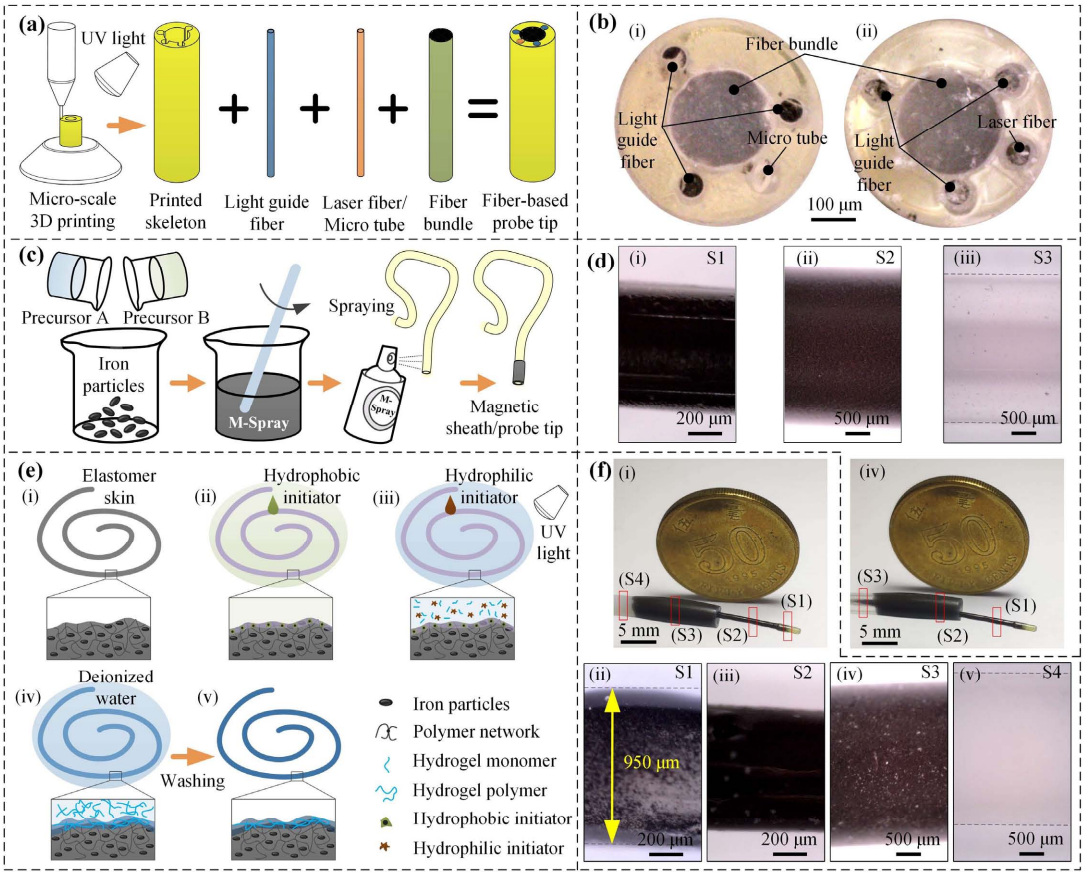

Figure S1. Schematic of the fabrication process for the magnetic continuum robot. (a) Schematic of microscale 3D printing procedure and the subsequent assembly step for the probe. (b) Top view of assembled probe tip with central fiber bundle, three light guide fibers, and functional tool of micro tube (b-i) and laser fiber (b-ii). (c) Schematic of the magnetic skin generation with M-spray. (d) The prototype of the probe and sheath with magnetic tip. The enlarged view (d-i), (d-ii), and (d-iii) are correspondingly denote the S1, S2, and S3 in subfigure (b-iv). (e) Schematic of the procedures for generating hydrogel skin on the outer surface of the probe/sheath. (f) The prototype of the magnetic probe/sheath coated with hydrogel layer. The enlarged view (f-ii), (f-iii), (f-iv), and (f-v) are correspondingly denote the S1, S2, S3 and S4 in subfigure (f-i).

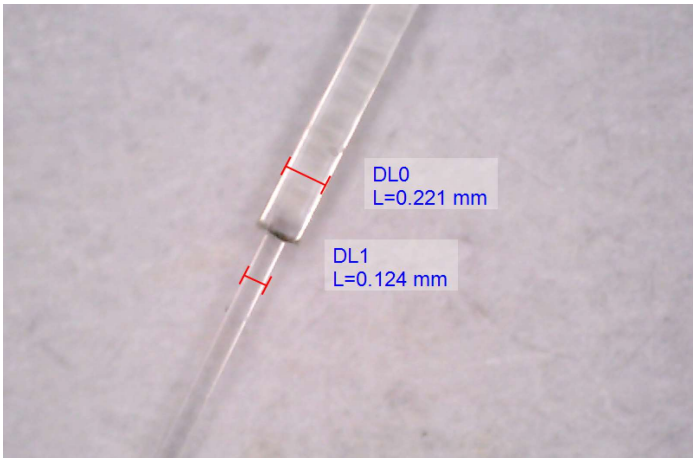

Figure S2. Contour measurement of the optical fiber utilized for transmitting medical cold light and the ablation laser.

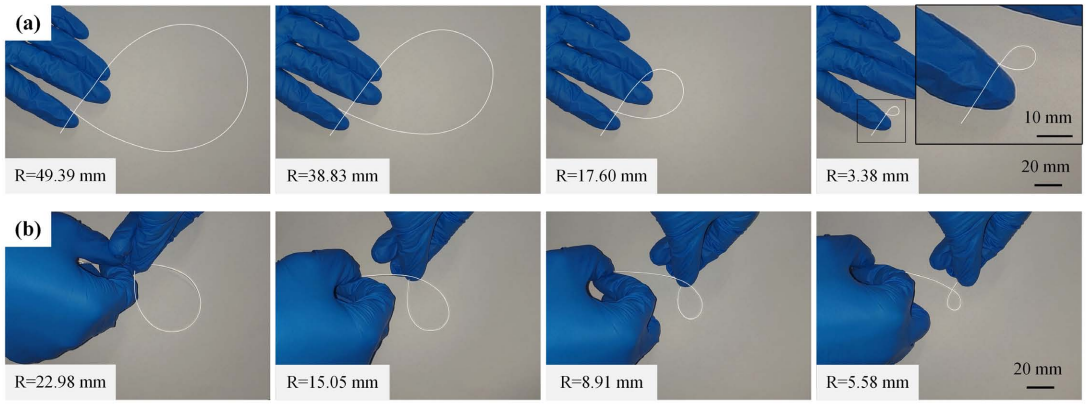

Figure S3. Bending performance of the optical fiber and the probe robot. (a-b) The bending performance of the optical fiber without the outer coating layer(a), and the assembled probe robot(b).

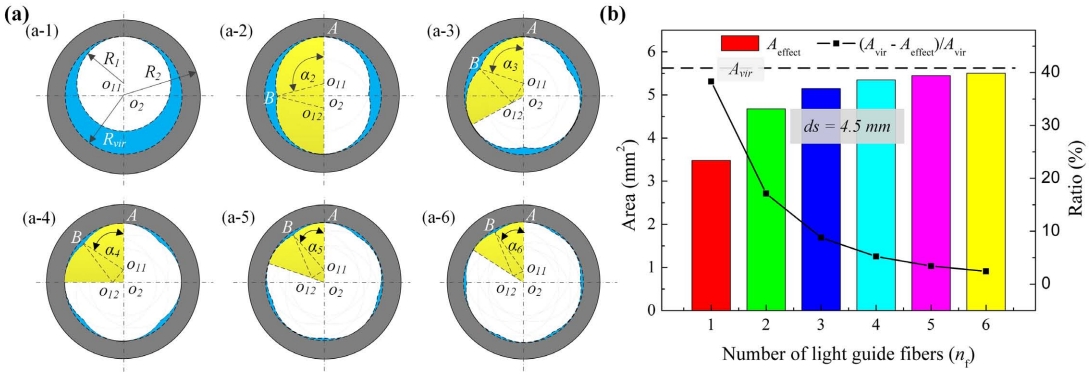

Figure S4. The theoretical analysis of the optical projection. (a) The theoretical imaging and light covering area against projection distance *ds* with the different skeleton structures. The gray and white area here correspond to the theoretical/effective projection region. The yellow and blue area here correspond to the $1/n_f$ effective projection and the difference between the effective and the virtual imaging region. (b) Statistical results of the theoretical ratio of the light covering over the imaging area with

different skeleton structures.

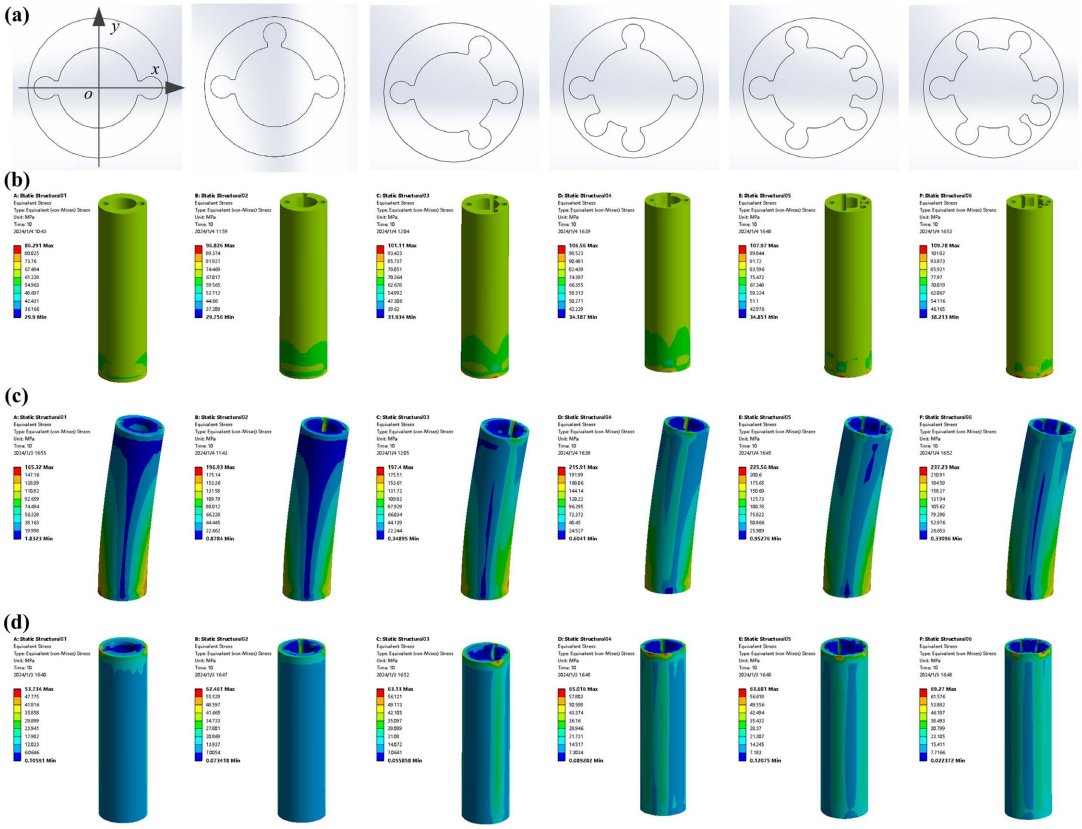

Figure S5. The mechanical strength simulation of the skeleton with the help of Finite Element Analysis (FEA). (a) Schematic of the top view of the skeleton with different structures, i.e., encapsulating the peripheral hole ranging from one to six. (b) The FEA results of the six skeletons under a normal load of 20.0 N. (c) The FEA results of the six skeletons under a lateral load of 2.0 N. (d) The FEA results of the six skeletons under a torque load of 0.5 N•mm.

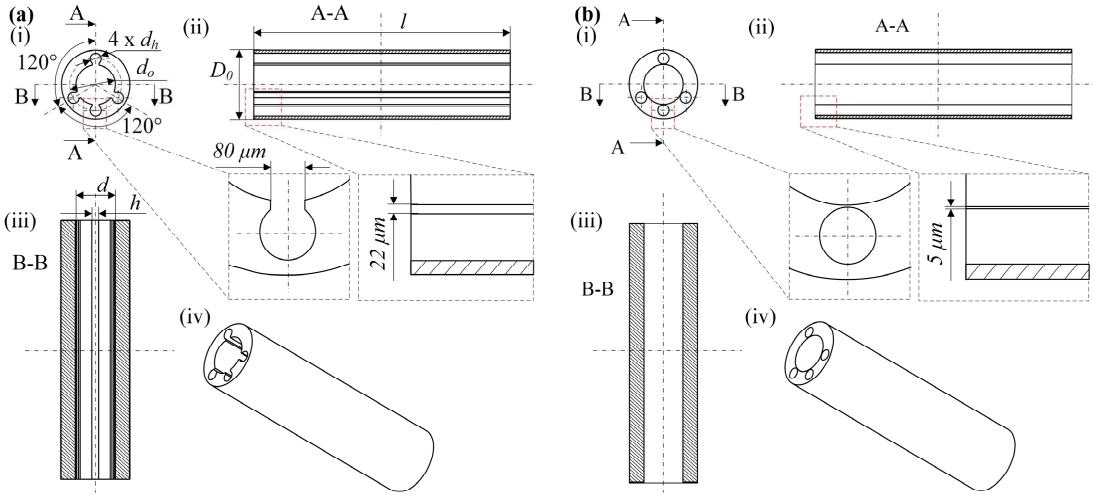

Figure S6. Structural comparison of the skeleton. (a,b) CAD model of the skeleton

with(a)/without(b) fillets resection. (i) Top view of the skeleton. (ii) A-A section view of the skeleton. (iii) B-B section view of the skeleton. (iv) Axonometric view of the skeleton.

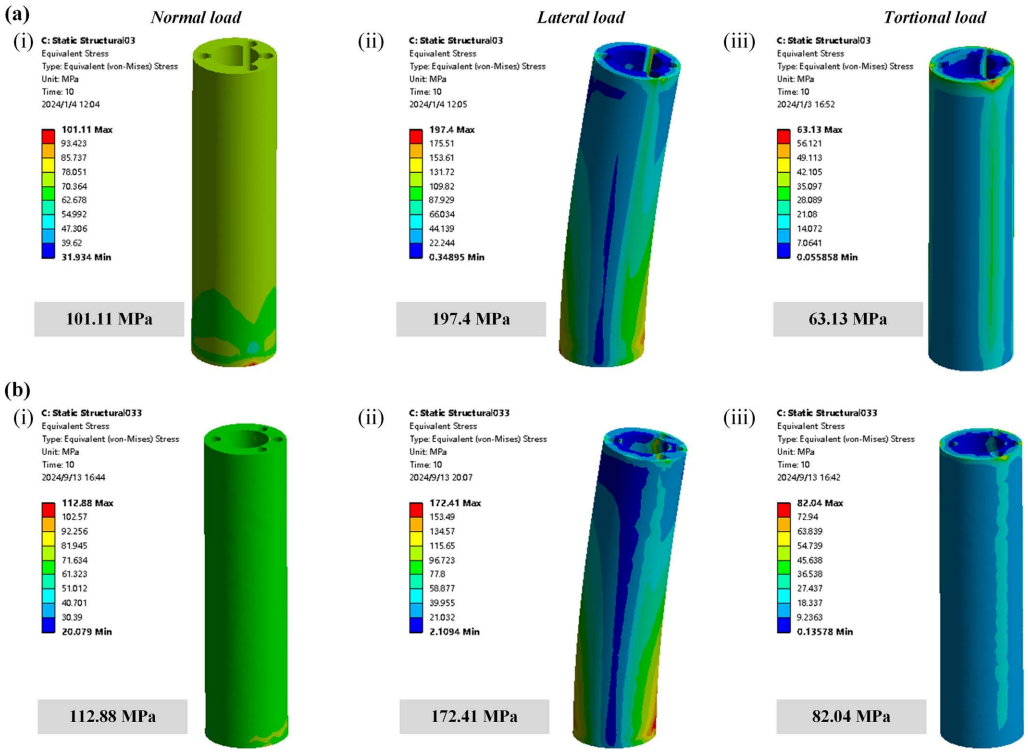

Figure S7. FEM mechanical simulation comparison of the skeleton. (a,b) FEM simulation results of the skeleton with(a)/without(b) fillets resection. (i) The result of the skeleton subjecting to a normal load of 20.0 N. (ii) The result of the skeleton subjecting to a lateral load of 2.0 N. (d) The result of the skeleton subjecting to a torque load of 0.5 N•mm.

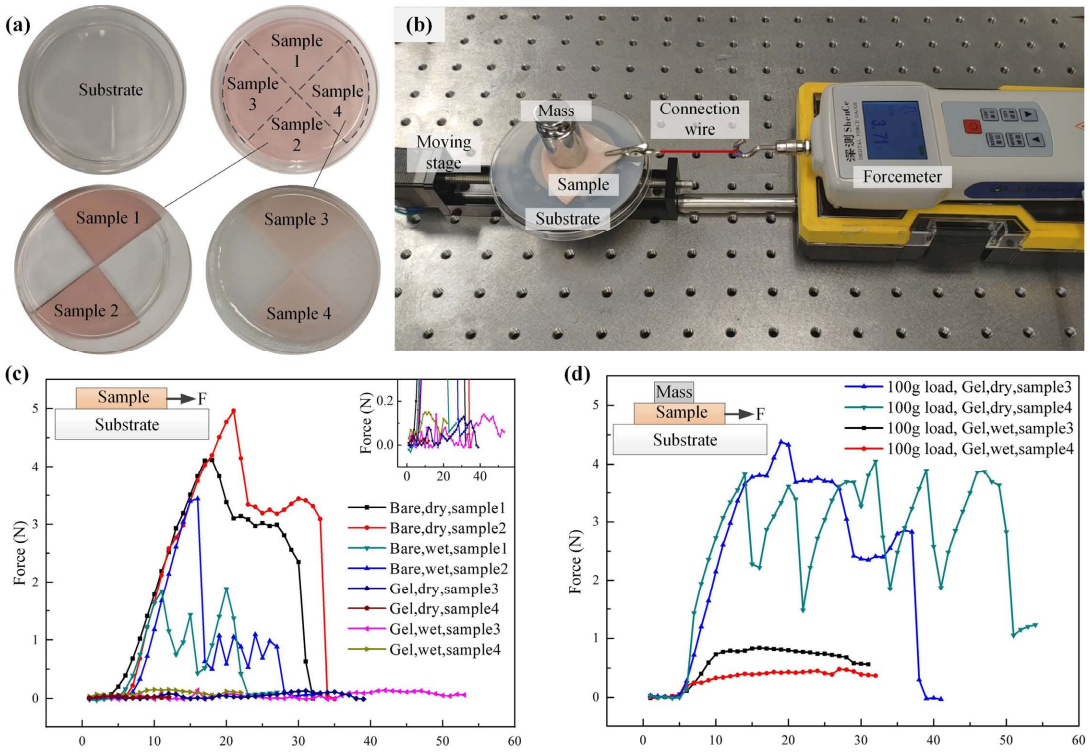

Figure S8. The sliding friction test of the elastomer with/without hydrogel formation. (a) The prepared substrate (pure elastomer) and samples (1,2 without hydrogel, 3,4 with hydrogel). (b) The experimental setup for testing the sliding friction. (c) The measured pulling force variation trend of samples with/without hydrogel formation under dry/wet environments. (d) The measured pulling force variation trend of samples with hydrogel skin under dry/wet environments while loading a 100 gram weights.

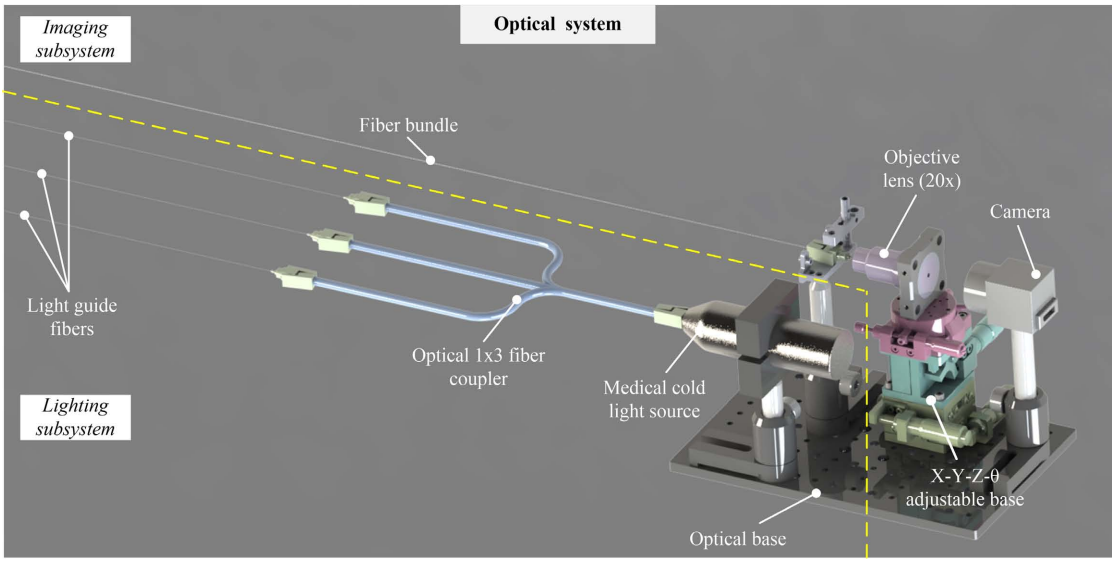

Figure S9. The 3D model of the endoscopic imaging system.

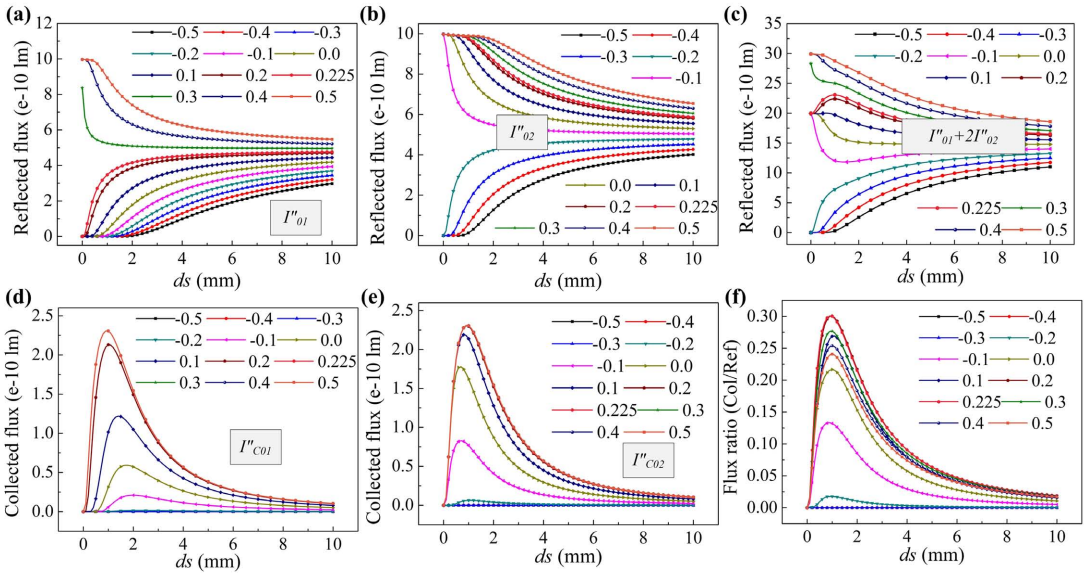

Figure S10. The theoretical analysis of the optical projection for the proposed probe. The theoretical reflected light flux from the first (a) /second (b) light guide fiber, under the condition that the reflective board is placed at a distance *ds* and lateral offset *dr* with respect to the central plane of the probe. (c) Sum of the reflected light flux from the three light guide fibers. The theoretical collected light flux from the first (d) /second (e) light guide fiber, under the condition that the reflective board is placed at a distance *ds* and lateral offset *dr* with respect to the central plane of the probe. (f) The theoretical light flux ratio (the collected flux over the reflected one) against both the distance *ds* and lateral offset *dr* distance *ds* and lateral offset *dr*.

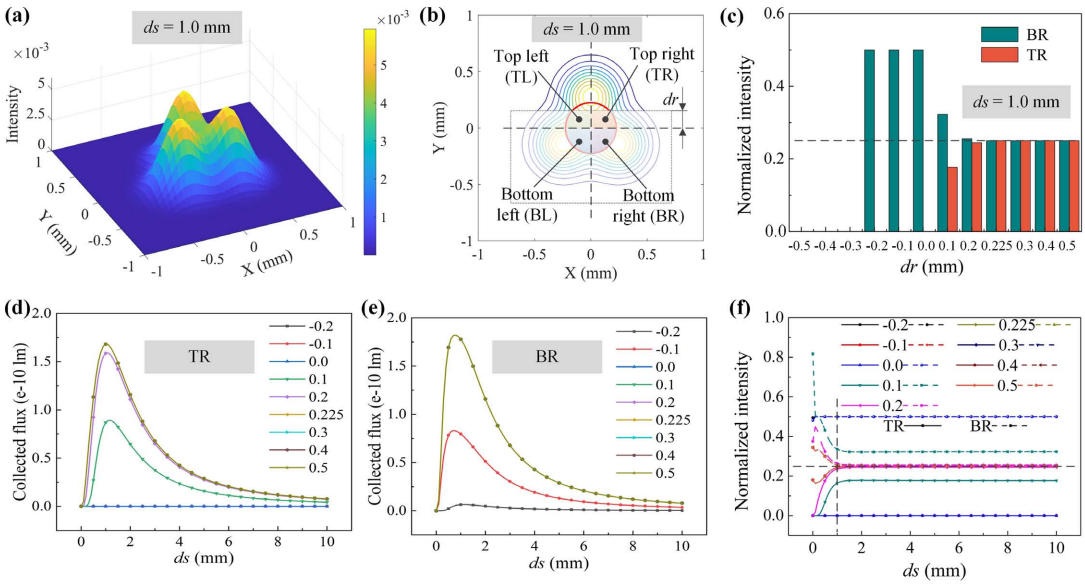

Figure S11. The theoretical analysis of the out-of-sight detection principle for the proposed probe. (a) The theoretical reflected light intensity distribution profile from the probe at a distance of *ds*=1.0 mm. (b) The corresponding contour map of the intensity

distribution. (c) The normalized intensity of the collected flux from the top right (TR) and bottom right (BR) quadrant of the central fiber bundle at the distance of *ds*=1.0 mm against lateral offset *dr*. (d, e, f) The theoretical intensity variation trend of the collected flux from the top right (TR) (d) and bottom right (BR) (e) quadrant of the central fiber bundle and the corresponding normalized values (f) against both the distance *ds* and the lateral offset *dr*.

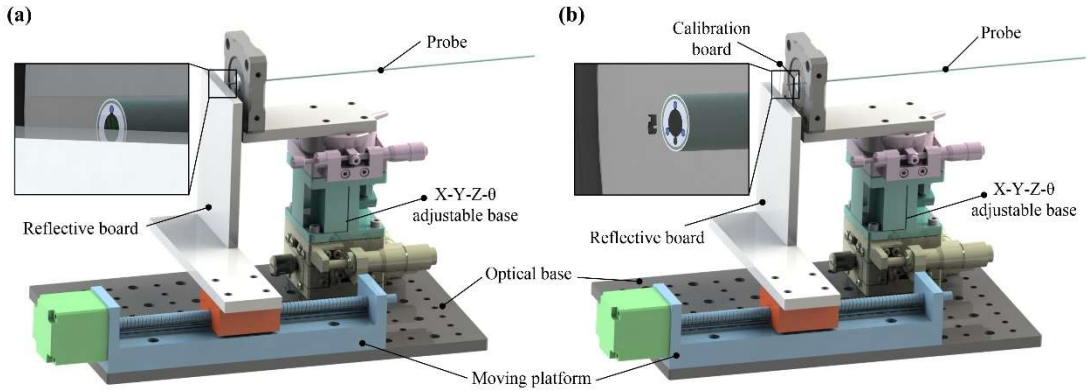

Figure S12. The experimental setup for characterizing the imaging capability of the proposed probe. (a) The testing setup for characterizing the collected intensity against both the distance *ds* and lateral offset *dr* of the reflective board. (b) The testing setup for characterizing the in situ imaging performance against the distance *ds* of the given pattern.

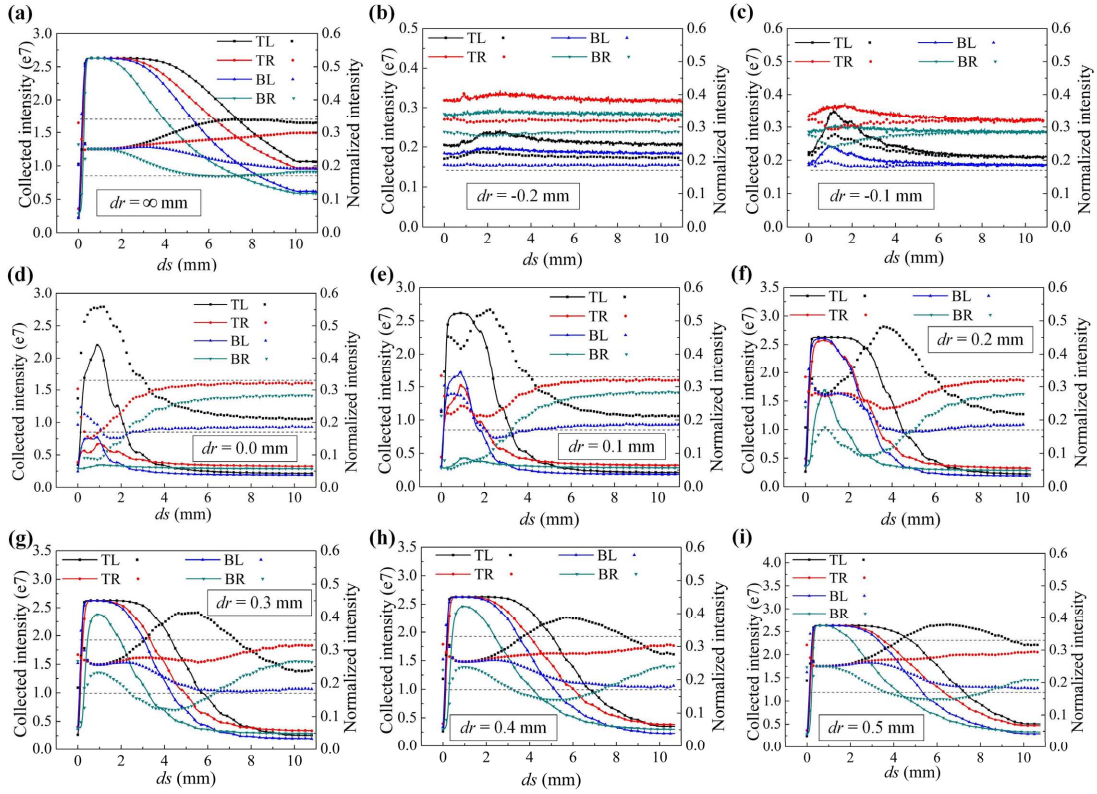

Figure S13. The normalized intensity difference between different areas in the view

against distance *ds* with different lateral offsets *dr*, e.g., (a) *dr* = ∞ mm, (b) *dr* = -0.2 mm, (c) *dr* = -0.1 mm, (d) *dr* = 0.0 mm, (e) *dr* = 0.1 mm, (f) *dr* = 0.2 mm, (g) *dr* = 0.3 mm, (h) *dr* = 0.4 mm, and (i) *dr* = 0.5 mm. TL, TR, BL, and BR represent top left, top right, bottom left, and bottom right, respectively.

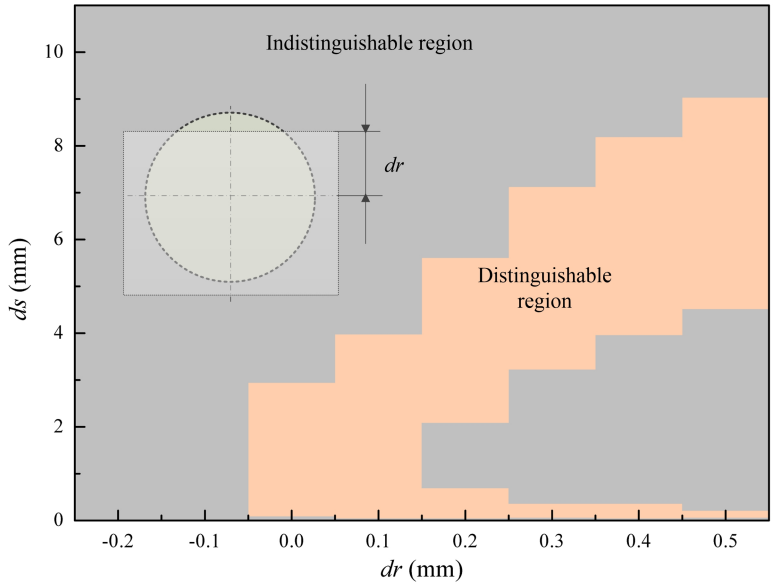

Figure S14. The statistical result of the out-of-sight obstacle detection performance against the lateral offset *dr* of the proposed probe.

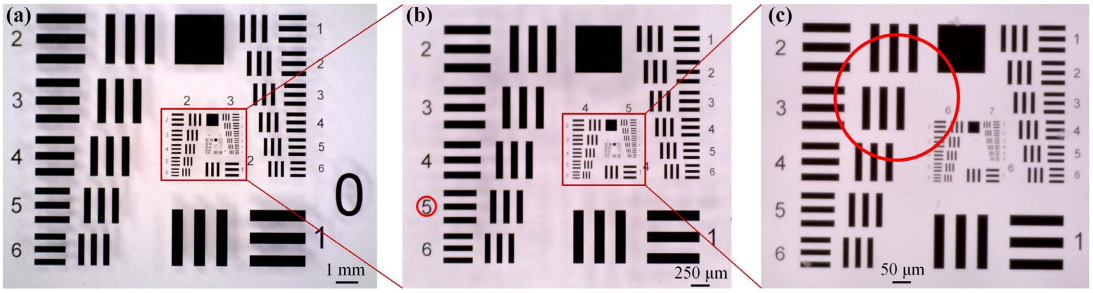

Figure S15. The calibration board utilized for characterizing imaging performance. (a) The whole image of the USAF 1951 calibration board, consisting of the resolution test chart of group 1 to 7. (b) The zoomed up image of the second/third group test chart. The number symbol "5" (labeled in a red circle) is then utilized for testing object recognition performance. (c) The zoomed up image of the fourth/fifth group test chart. The circled area is then employed for testing the imaging resolution.

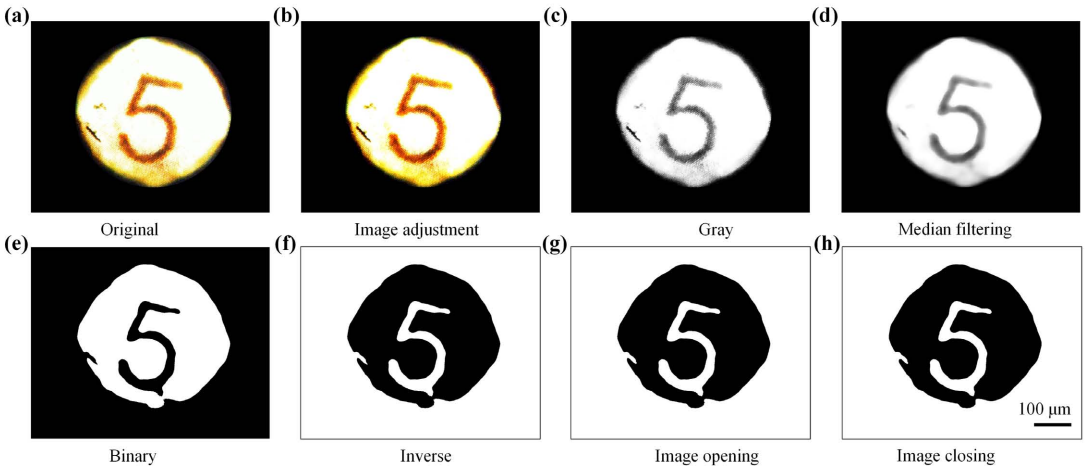

Figure S16. The imaging processing procedures for segmenting the contour of the captured object. (a) The captured image of the number symbol '5' under an exposure duration of 30 ms with zero distance. (b) The result after image adjustment for enhancing contrast. (c) The obtained grayscale image of the adjusted one for processing simplification. (d) The result after a median filtering for initially removing noises. (e) The result after the image binary operation for further simplification. (f) The result after the image inverse operation. (g) The result after an opening processing for removing the pixel connections between the target and the noises. (h) The final result after an image closing procedure for object segmentation.

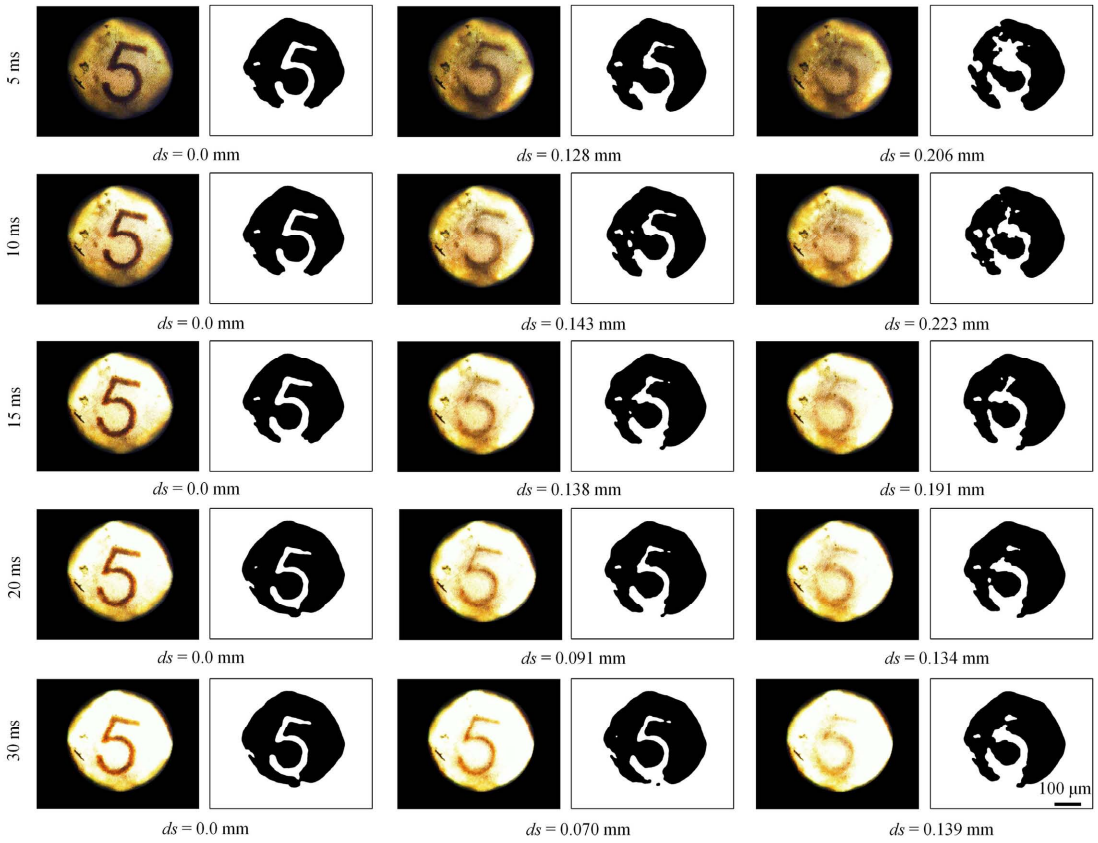

Figure S17. The target segmentation results for confirming the distance range of clear/obscure recognition under diverse exposure durations.

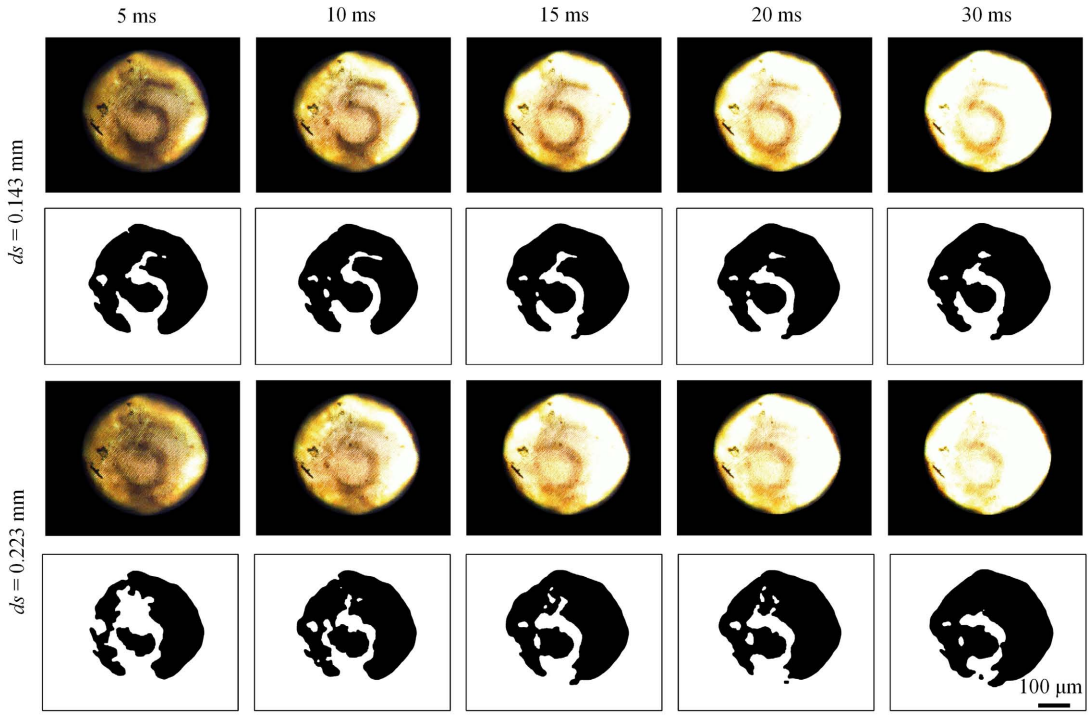

Figure S18. The target segmentation results at three specific distances under diverse exposure durations.

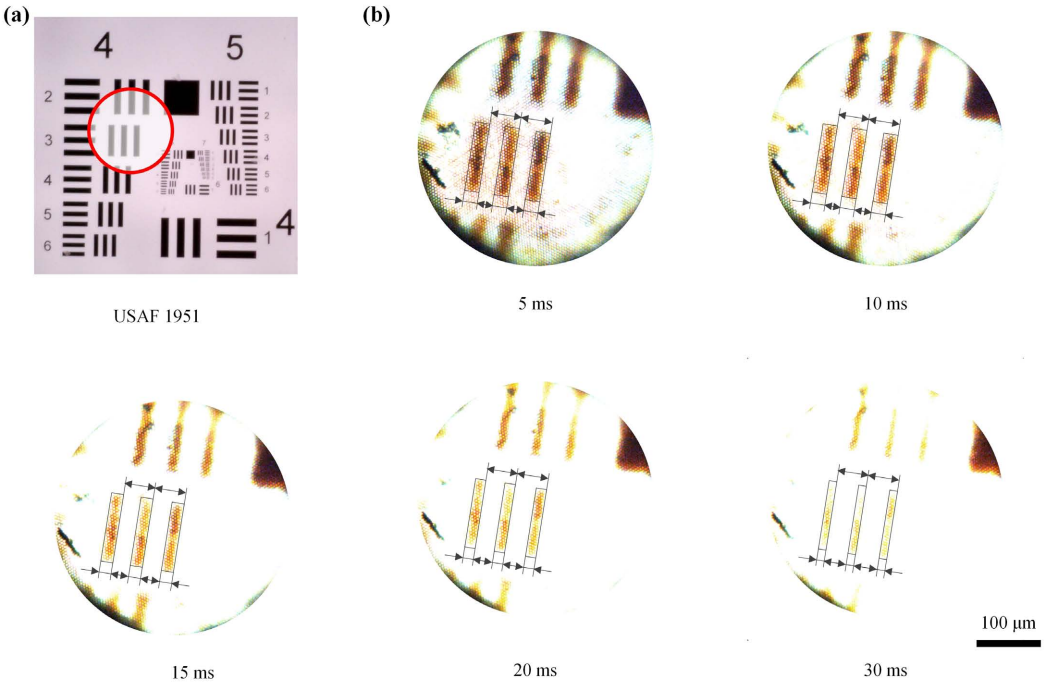

Figure S19. The comparison of imaging resolution results under different exposure

duration conditions. (a) The schematic of the utilized USAF 1951 resolution test chart. The red circle denotes the experimental area. (b) The experimental results for investigating the imaging resolution.

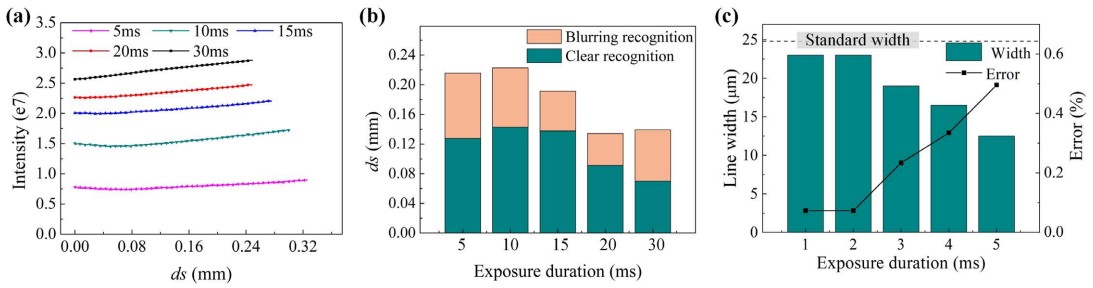

Figure S20. The statistical results of imaging performance of the proposed probe. (a) The recorded intensity variation against the distance *ds* under different exposure duration conditions. (b) The statistical results of the clear/blurring recognition region under different exposure durations. (c) The statistical results of the imaging resolution under different exposure durations.

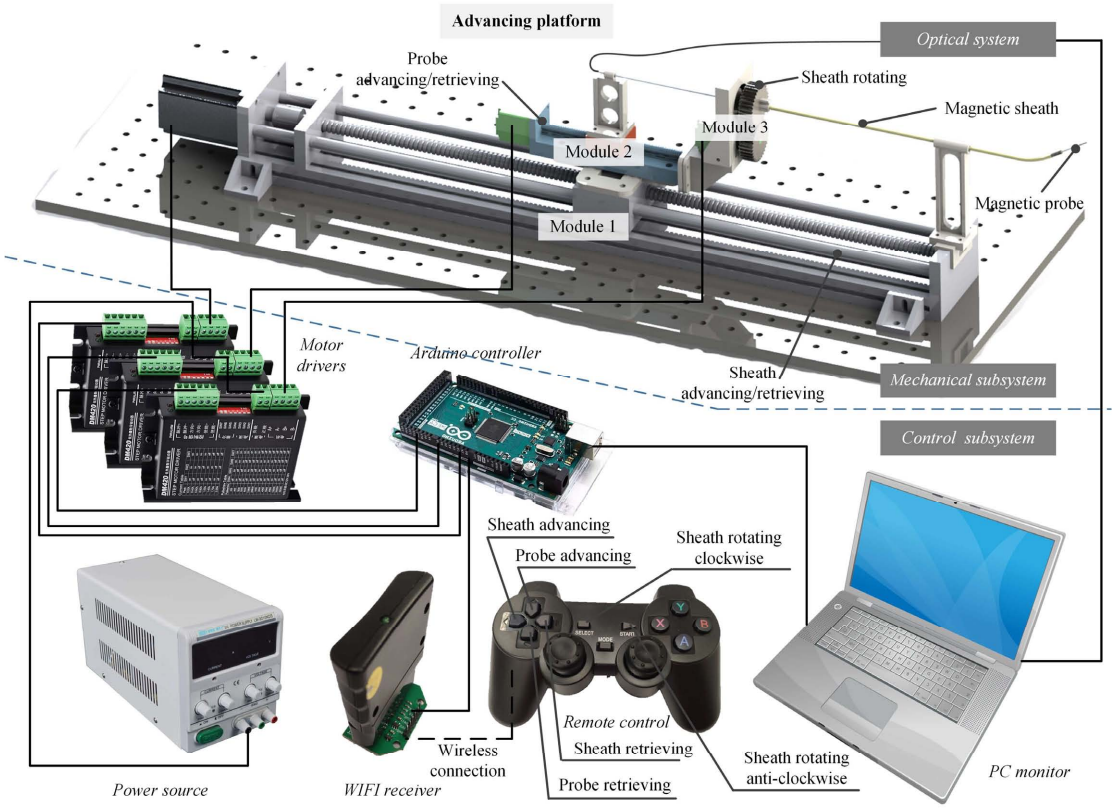

Figure S21. The back-end advancing platform for achieving a smooth intervention with the soft sheath and the probe integrated.

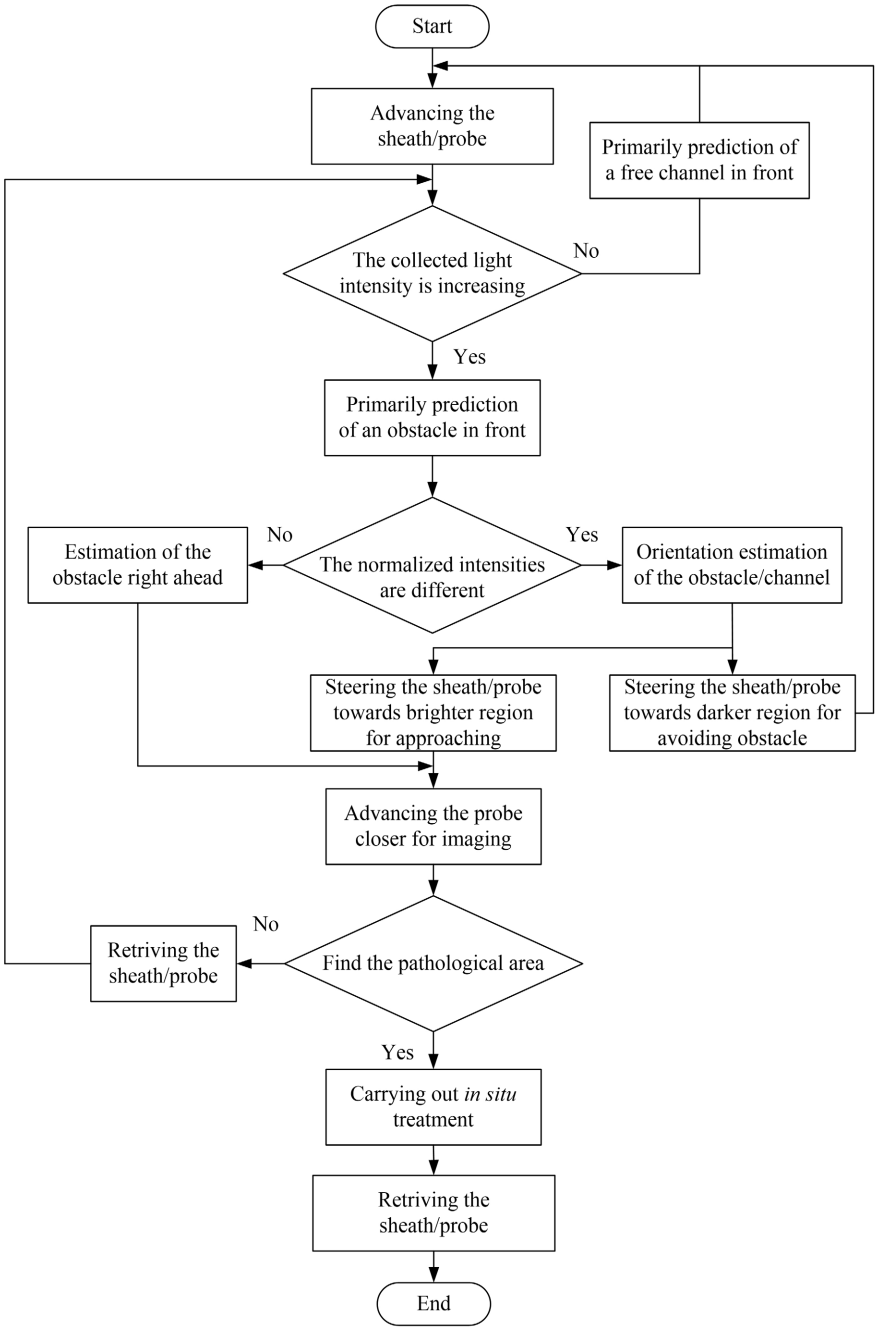

Figure S22. The interventional surgery procedure based on the proposed intensity distribution-based environment exploration strategy.

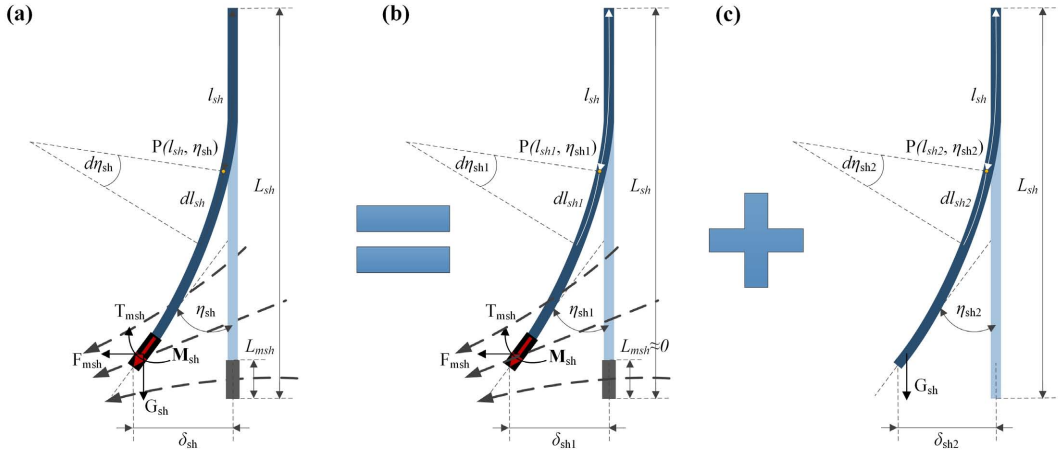

Figure S23. The deformation model of the sheath under the applied gradient magnetic field. (a) The soft sheath with a magnetic tip actuated by gradient magnetic field while experiencing gravity. (b) The soft sheath with a magnetic tip actuated by gradient magnetic field without gravity. (c) The soft sheath with pure rubber body subjects only gravity.

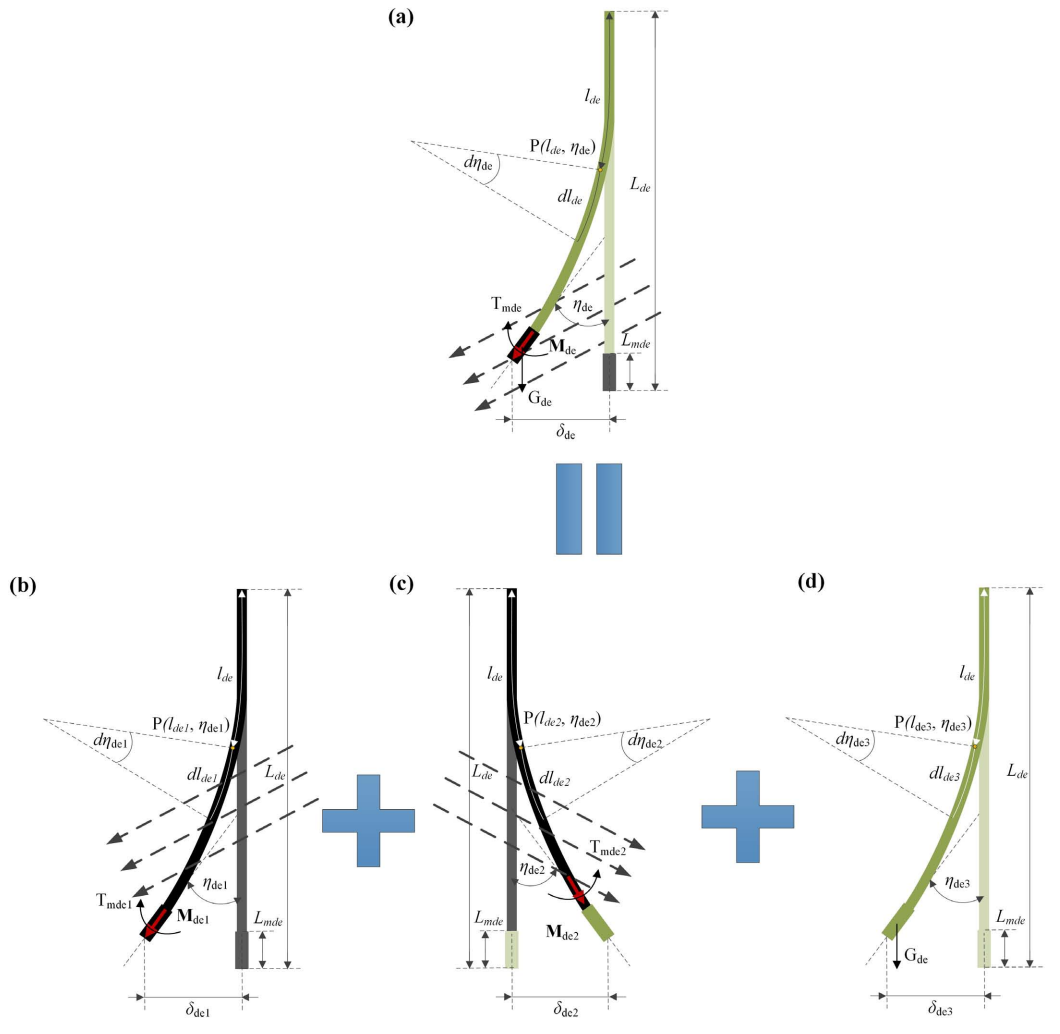

Figure S24. The deformation model of the probe under the applied uniform magnetic field. (a) The probe with a magnetic tip actuated by uniform magnetic field while experiencing gravity. (b) The probe with an entire magnetic body actuated by uniform magnetic field without gravity. (c) The probe with a certain length (L_{de} - L_{mde}) of magnetic body actuated by uniform magnetic field without gravity. (d) The probe without magnetic components subjects only gravity.

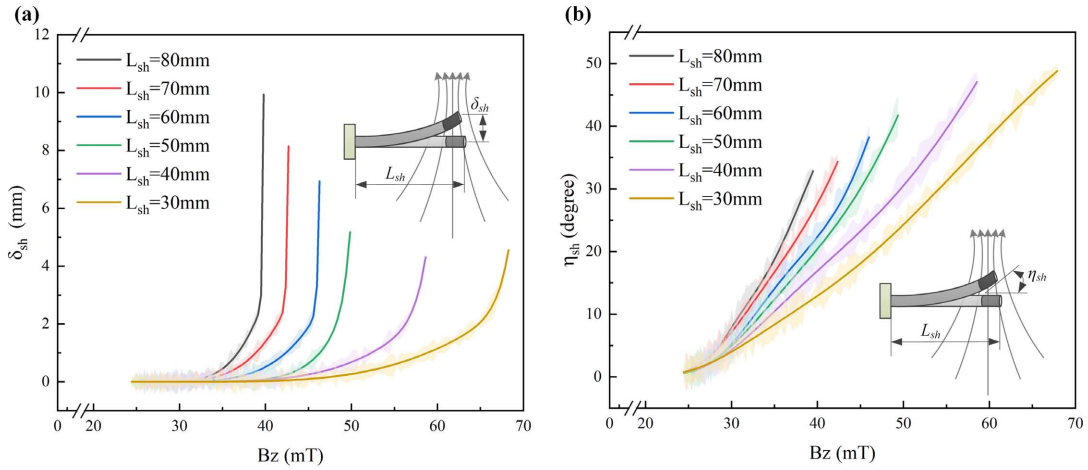

Figure S25. Characterization of the magnetic response of the magnetic sheath. (a, b) The deformation (a) and the corresponding bending angle (b) of the magnetic sheath with different beam length under the magnetic actuation. Data are represented as mean values ± s.d. from three samples.

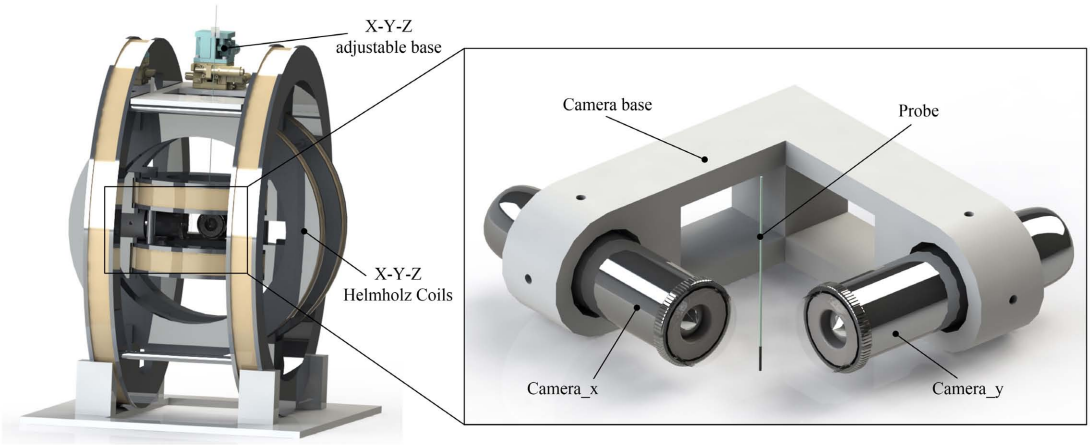

Figure S26. The 3D model of the three-degree-of-freedom (3DOF) Helmholtz coil system for actuating the magnetic probe and the integrated vertical perspective recording system for tracking the probe tip's movement.

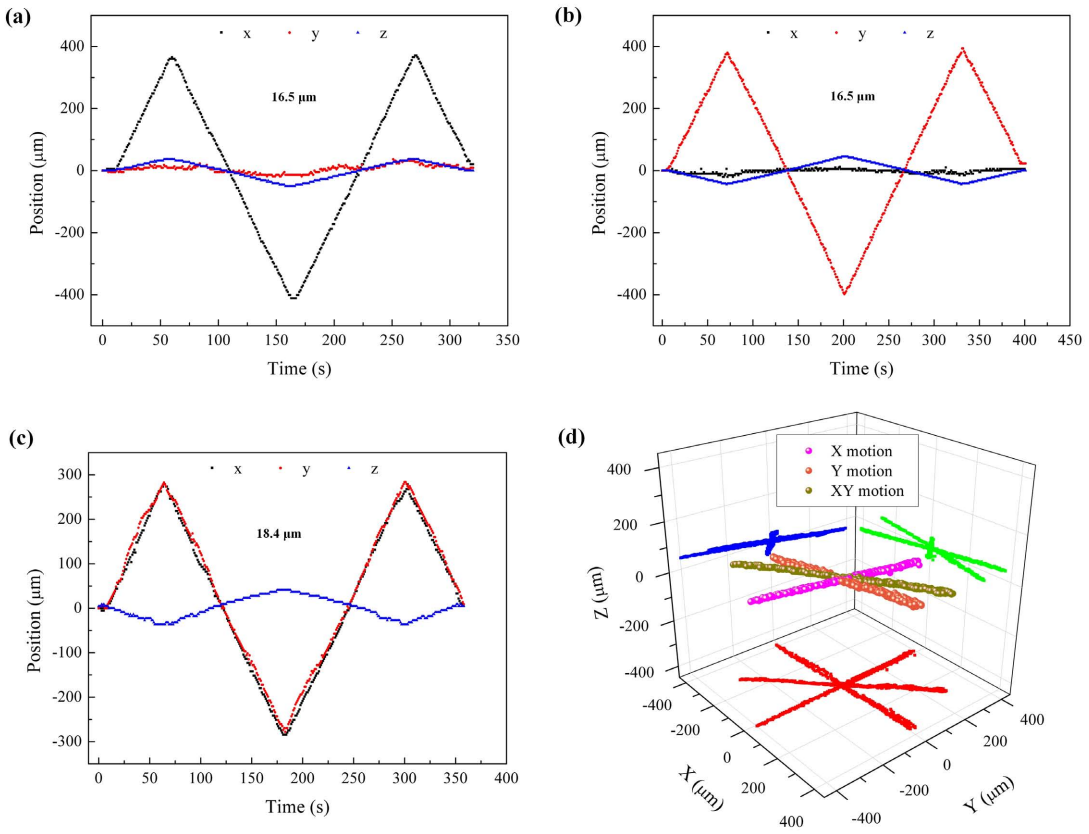

Figure S27. Characterization of linear motion under the magnetic actuation. (a) The recorded displacement in the 3D space for a linear motion along x axis. (b) The recorded displacement in the 3D space for a linear motion along y axis. (c) The recorded displacement in the 3D space for a linear motion along the direction of 45 degrees with x axis. (d) The reconstructed trajectories of the three types of linear motion. The red, green, and blue dots here correspond to the projection in the x-o-y plane, x-o-z plane, and y-o-z plane of the recorded trajectories.

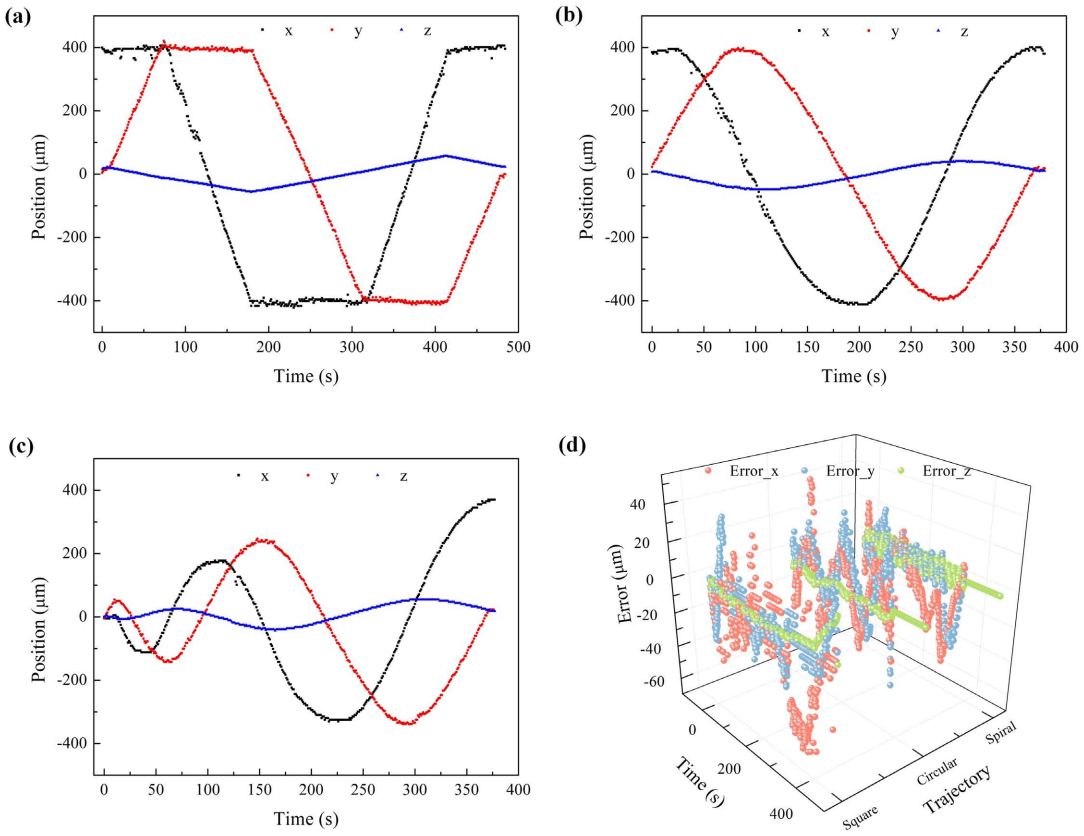

Figure S28. Characterization of complex motion under the magnetic actuation. (a) The recorded displacement in the 3D space for a square motion. (b) The recorded displacement in the 3D space for a circular motion. (c) The recorded displacement in the 3D space for a spiral motion. (d) The tracking errors of the three types of complex motion.

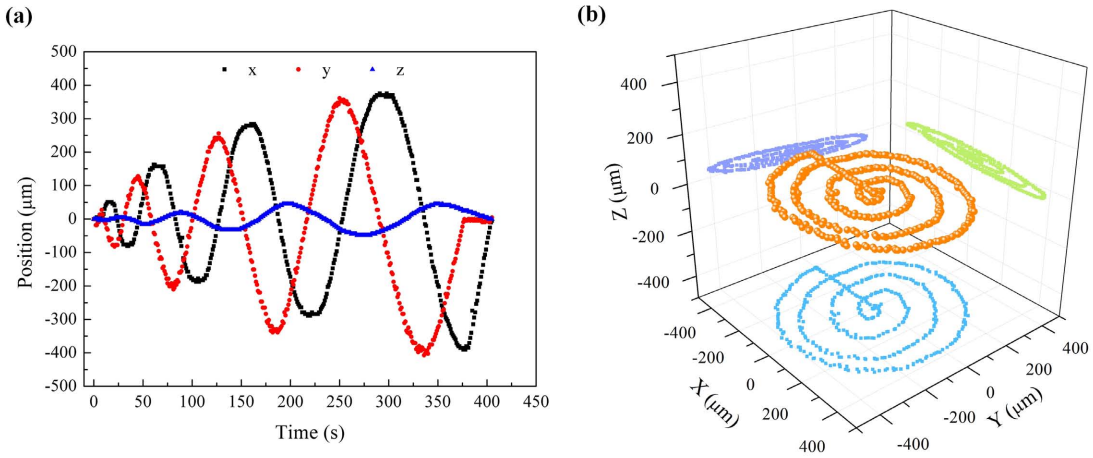

Figure S29. The Archimedes spiral trajectory designed for carrying out the scanning imaging. (a) The recorded displacement in the 3D space for the spiral motion. (b) The reconstructed trajectories of the spiral motion. The light blue, green, and purple dots here correspond to the projection in the x-o-y plane, x-o-z plane, and y-o-z plane of the recorded trajectories.

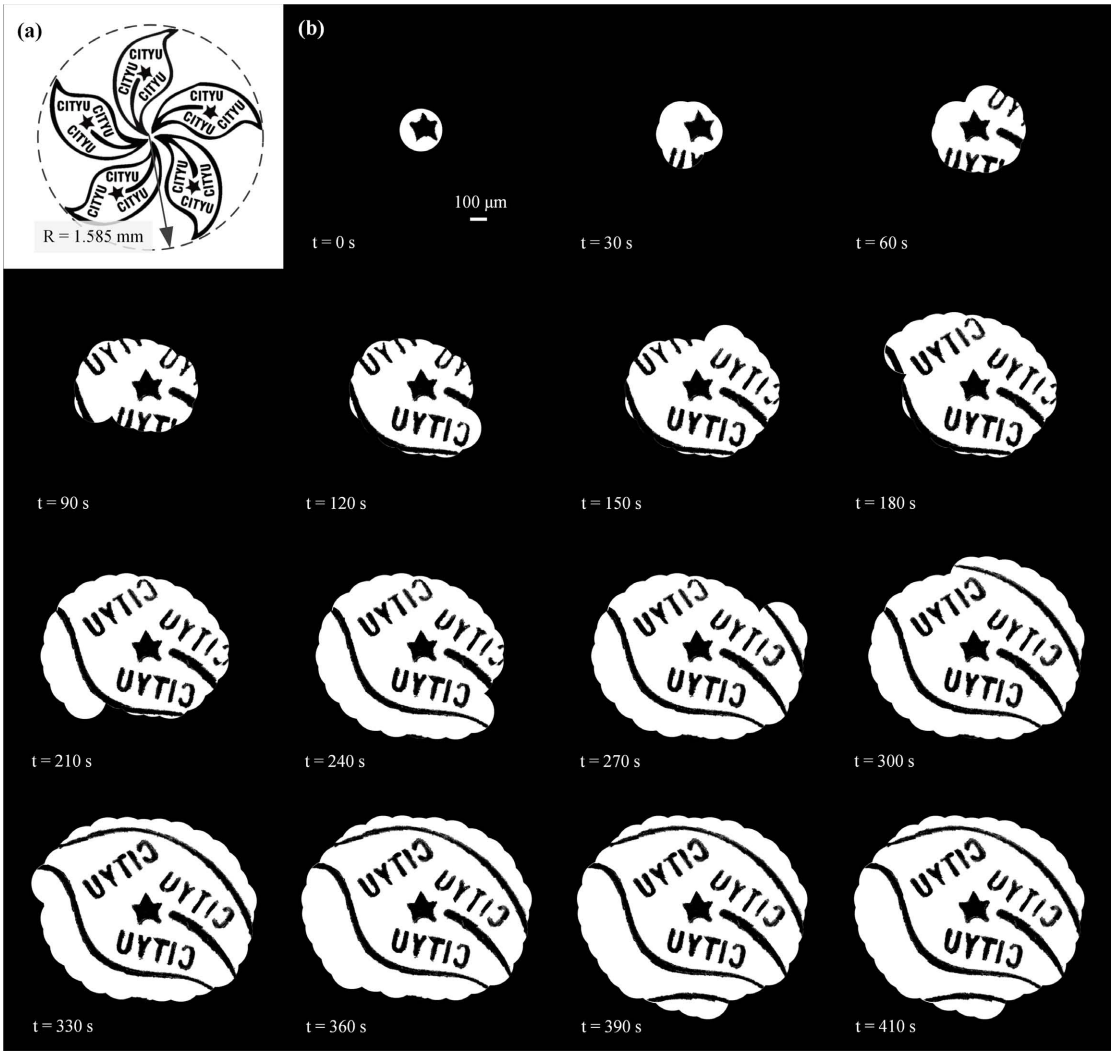

Figure S30. The scanning imaging result of a bauhinia flower pattern. (a) Schematic of the bauhinia flower pattern with a diameter of 3.17 mm. (b) The accumulated scanning imaging effect at different time.

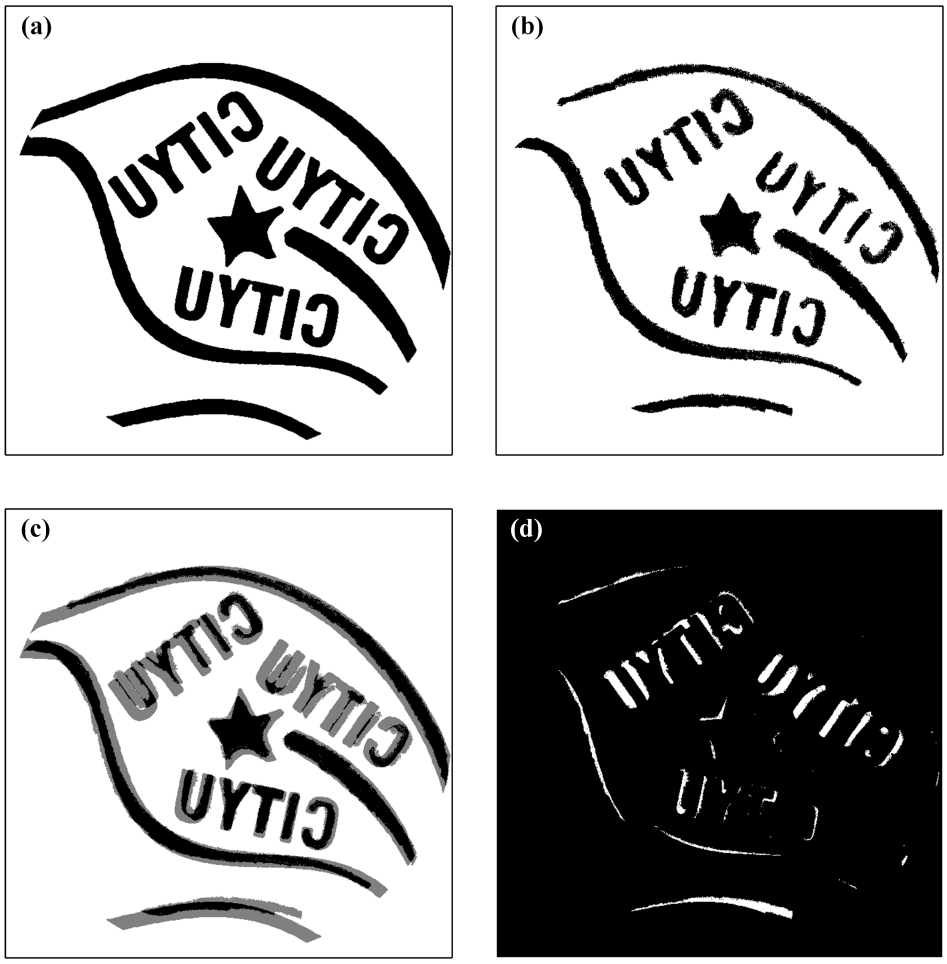

Figure S31. The comparison between the given pattern and the reconstructed image. (a) The theoretical region of the given pattern that the probe should scanning. (b) The stitched image after the scanning process. (c) The overlap comparison between the two images. (d) The difference between the two images.

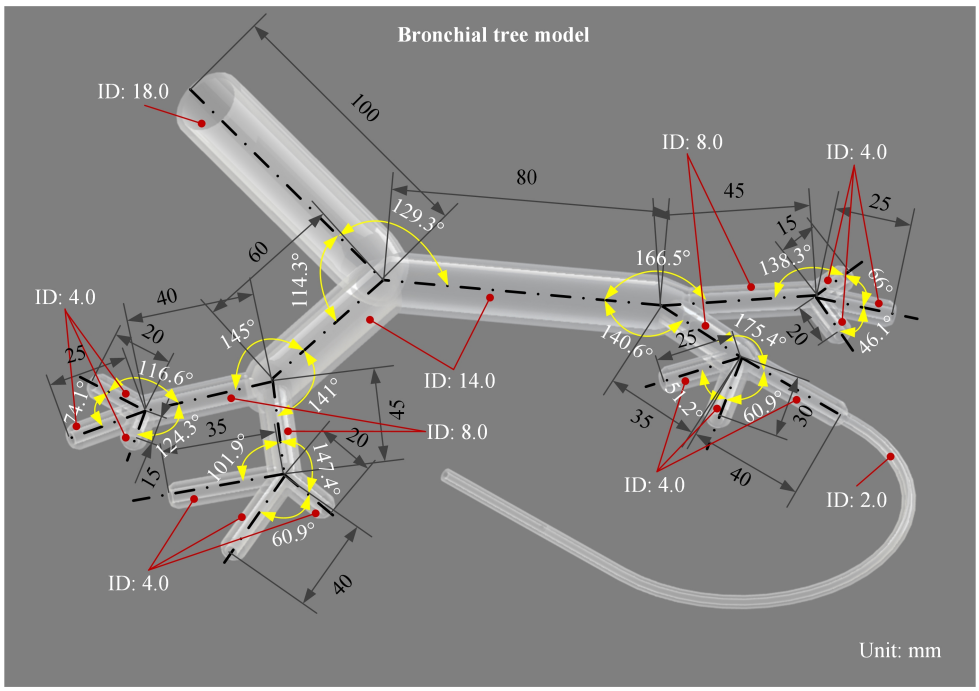

Figure S32. The dimensional schematic of the printed lung bronchial tree model.

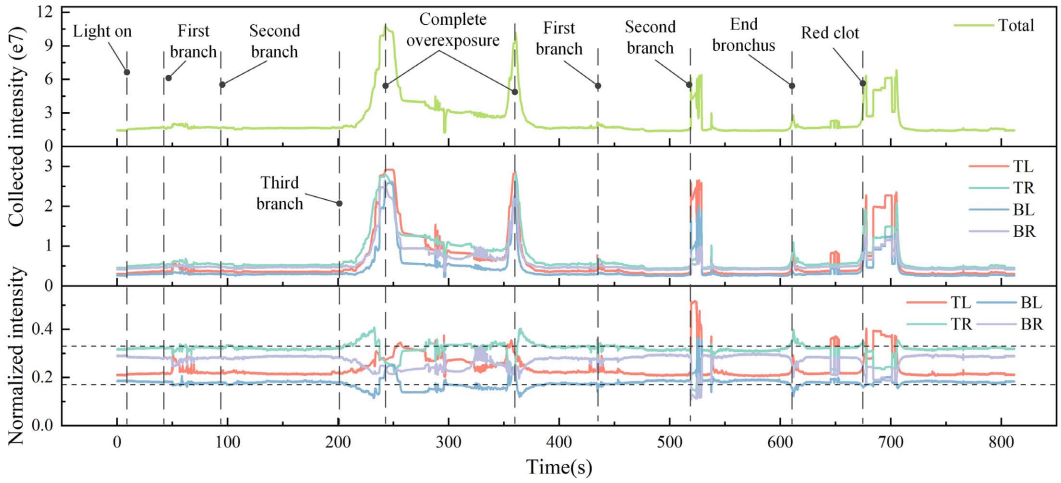

Figure S33. The recorded intensity variation during the interventional process inside the in vitro lung bronchial tree model. TL, TR, BL, and BR represent top left, top right, bottom left, and bottom right, respectively.

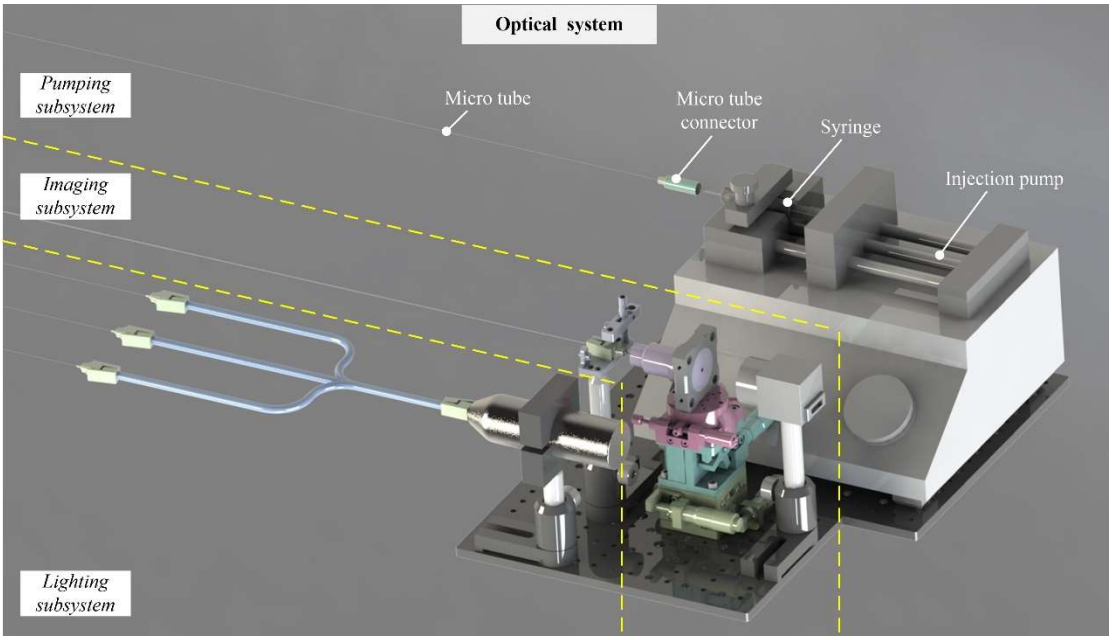

Figure S34. The 3D model of the established pumping subsystem for liquid delivery.

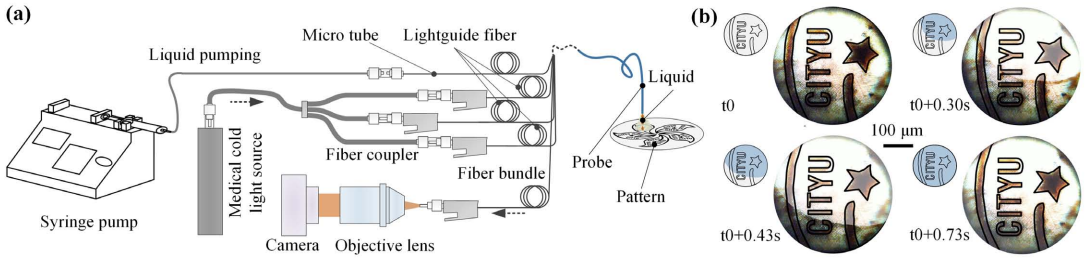

Figure S35. The experimental result of endoscopic liquid delivery. (a) Schematic of the endoscopic liquid delivery on a given pattern. (b) The endoscopic recordings that verify the successful delivery of droplet.

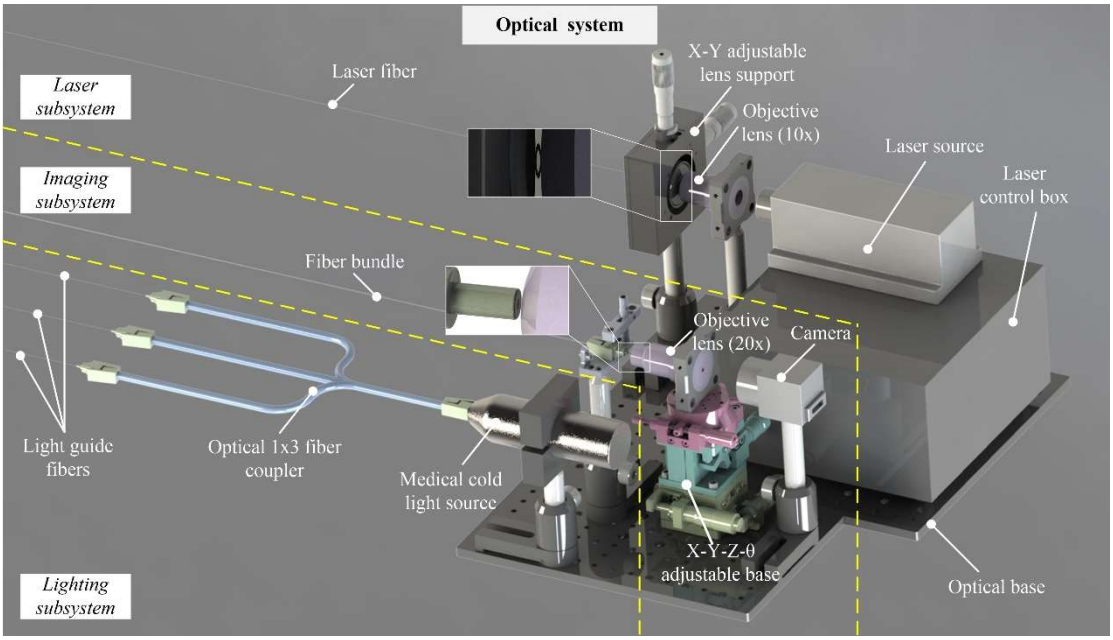

Figure S36. The 3D model of the established laser subsystem for laser delivery.

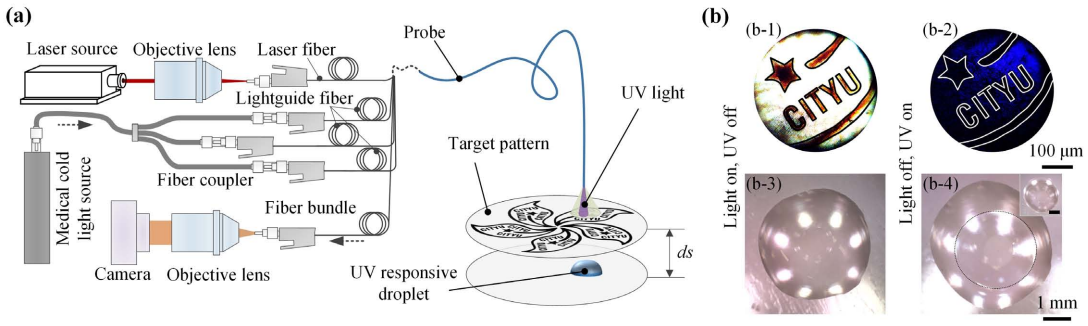

Figure S37. The experimental result of endoscopic laser delivery. (a) Schematic of the endoscopic laser delivery on a given pattern. (b) The endoscopic recordings and microscopic results that verify the successful delivery of UV laser.

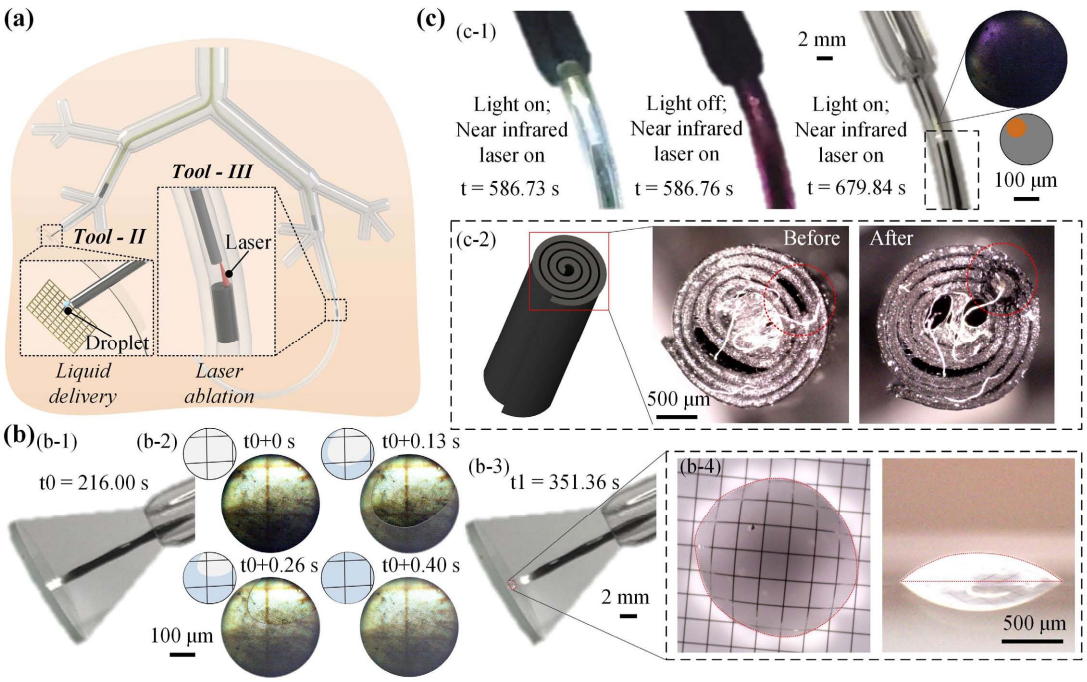

Figure S38. The in vitro interventional experiments for demonstrating the in situ functional operations with the proposed continuum robot. (a) Schematic of the liquid delivery and laser ablation inside a printed lung bronchial tree model. (b) The endoscopic recordings and microscopic results that verify the successful delivery of droplet on a grid pattern. (c) The endoscopic recordings and microscopic results that verify the successful delivery of near-infrared laser (NIL: 808 nm) on a coiled electrical tape.

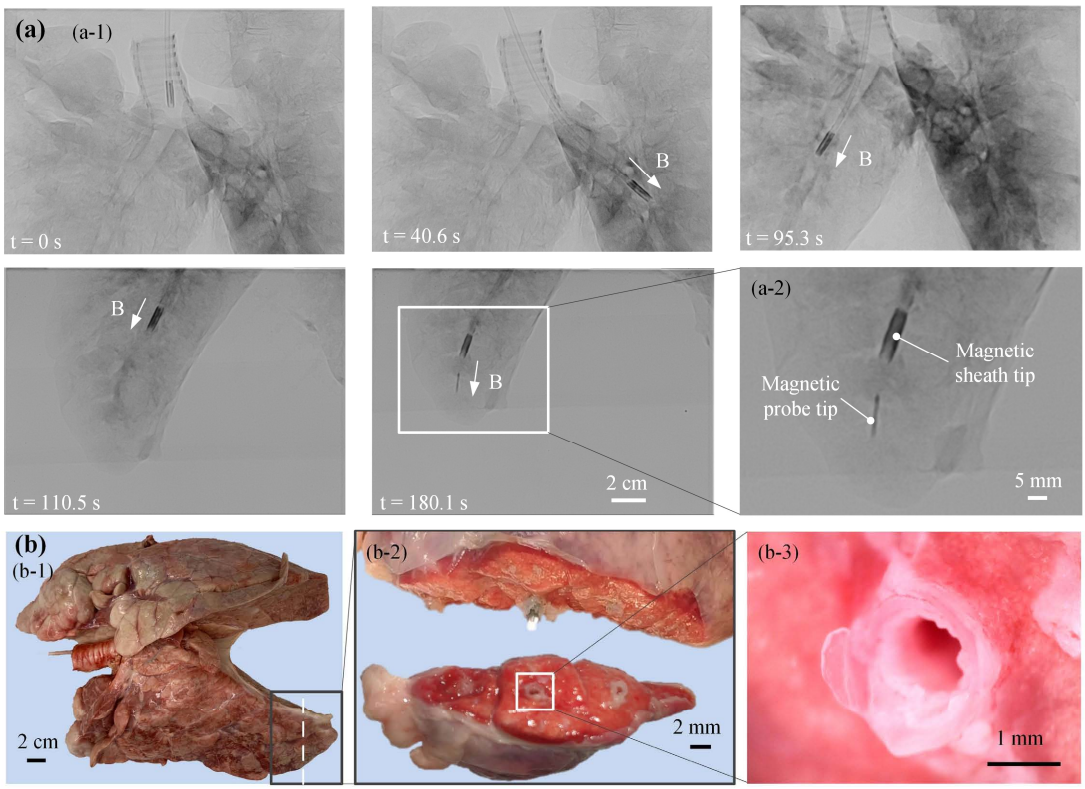

Figure S39. The interventional experiment inside an ex vivo porcine lung (sample I). (a) The DSA results that verify the successful accessing process of the proposed continuum robot. (b) The anatomical examination for validating the small diameter of the end bronchus.

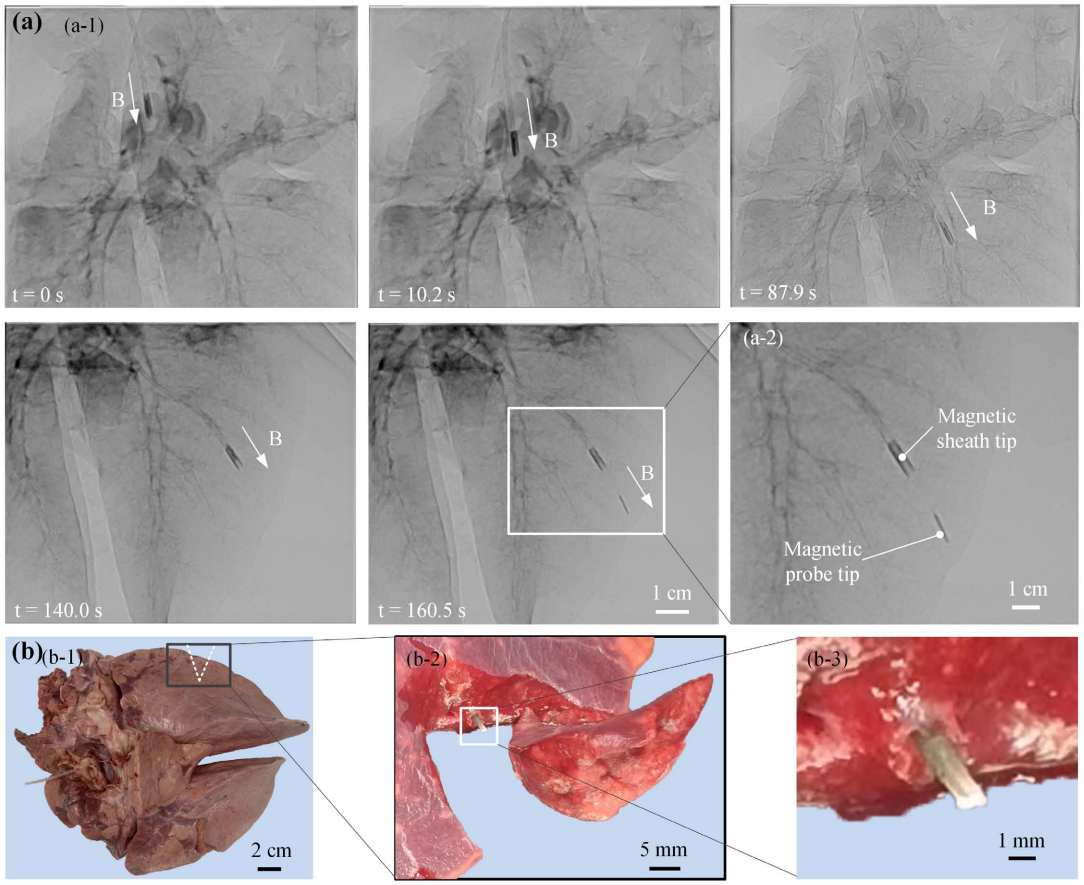

Figure S40. The interventional experiment inside an ex vivo porcine lung (sample II). (a) The DSA results that verify the successful accessing process of the proposed continuum robot. (b) The anatomical examination for validating the small diameter of the end bronchus.

Supplementary References

[1] Yang, X., Shang, W., Lu, H., Liu, Y., Yang, L., Tan, R., ... & Shen, Y. (2020). An agglutinate magnetic spray transforms inanimate objects into millirobots for biomedical applications. *Science robotics*, *5*(48), eabc8191.

[2] Loh, J. M., Lim, Y. J. L., Tay, J. T., Cheng, H. M., Tey, H. L., & Liang, K. (2024). Design and fabrication of customizable microneedles enabled by 3D printing for biomedical applications. *Bioactive Materials*, *32*, 222-241.

[3] Xiao, R., Feng, X., Liu, W., Zhou, W., Li, X., Song, I., ... & Lu, Y. (2023). Direct 3D printing of thin-walled cardiovascular stents with negative Poisson's ratio (NPR) structure and functional metallic coating. *Composite Structures*, *306*, 116572.

[4] Cheng, X., Li, W., Yuan, J., & Wang, S. (2023). Simultaneously Enhanced Chain Flexibility, Three Dimensional Printability, and Reduction of Shrinkage Stress in Biodegradable and Photocurable Multiblock Copolymers. *Macromolecules*, *56*(10), 3550-3561.

[5] Zare, M., Ghomi, E. R., Venkatraman, P. D., & Ramakrishna, S. (2021). Silicone-based biomaterials for biomedical applications: antimicrobial strategies and 3D printing technologies. *Journal of applied polymer science*, *138*(38), 50969.

[6] del Bosque, A., Sánchez-Romate, X. F., Gómez, A., Sánchez, M., & Ureña, A. (2023). Highly stretchable strain sensors based on graphene nanoplatelet-doped ecoflex for biomedical purposes. *Sensors and Actuators A: Physical*, *353*, 114249.

[7] Sparks, J. L., Vavalle, N. A., Kasting, K. E., Long, B., Tanaka, M. L., Sanger, P. A., ... & Conner-Kerr, T. A. (2015). Use of silicone materials to simulate tissue biomechanics as related to deep tissue injury. *Advances in skin & wound care*, *28*(2), 59-68.

[8] Yu, Y., Yuk, H., Parada, G. A., Wu, Y., Liu, X., Nabzdyk, C. S., ... & Zhao, X. (2019). Multifunctional "hydrogel skins" on diverse polymers with arbitrary shapes. *Advanced Materials*, *31*(7), 1807101.

[9] Choi, W., Kang, M., Hong, J. H., Katz, O., Lee, B., Kim, G. H., ... & Choi, W. (2022). Flexible-type ultrathin holographic endoscope for microscopic imaging of unstained biological tissues. *Nature communications*, *13*(1), 4469.

[10] Gifari, M. W., Naghibi, H., Stramigioli, S., & Abayazid, M. (2019). A review on recent advances in soft surgical robots for endoscopic applications. *The International Journal of Medical Robotics and Computer Assisted Surgery*, *15*(5), e2010.

[11] Song, Y., Wang, S., Luo, X., & Shi, C. (2022). Design and optimization of a 3D printed distal flexible joint for endoscopic surgery. *IEEE Transactions on Medical Robotics and Bionics*, *4*(1), 38-49.

[12] https://www.fiberscope.net/ultra-fine-micro-borescope/

[13] https://aitproducts.com/wiki/flexible_borescope_bending_radius.html

[14] Kiesslich, R., Goetz, M., Hoffman, A., & Galle, P. R. (2011). New imaging techniques and opportunities in endoscopy. *Nature reviews Gastroenterology & hepatology*, *8*(10), 547-553.

[15] Subramanian, V., & Ragunath, K. (2014). Advanced endoscopic imaging: a review of commercially available technologies. *Clinical Gastroenterology and Hepatology*, *12*(3), 368-376.